ISSN 8755-6839

SCIENCE OF **TSUNAMI HAZARDS**

Journal of Tsunami Society International

Volume 32 **Number 2** **2013**

TSUNAMI SOCIETY INTERNATIONAL, 1741 Ala Moana Blvd. #70, Honolulu, HI 96815, USA.

SCIENCE OF TSUNAMI HAZARDS is a CERTIFIED OPEN ACCESS Journal included in the prestigious international academic journal database DOAJ, maintained by the University of Lund in Sweden with the support of the European Union. SCIENCE OF TSUNAMI HAZARDS is also preserved, archived and disseminated by the National Library, The Hague, NETHERLANDS, the Library of Congress, Washington D.C., USA, the Electronic Library of Los Alamos, National Laboratory, New Mexico, USA, the EBSCO Publishing databases and ELSEVIER Publishing in Amsterdam. The vast dissemination gives the journal additional global exposure and readership in 90% of the academic institutions worldwide, including nation-wide access to databases in more than 70 countries.

OBJECTIVE: Tsunami Society International publishes this interdisciplinary journal to increase and disseminate knowledge about tsunamis and their hazards.

DISCLAIMER: Although the articles in SCIENCE OF TSUNAMI HAZARDS have been technically reviewed by peers, Tsunami Society International is not responsible for the veracity of any statement, opinion or consequences.

Submit manuscripts of research papers, notes or letters to the Editor. If a research paper is accepted for publication the author(s) must submit a scan-ready manuscript, a Doc, TeX or a PDF file in the journal format. Issues of the journal are published electronically in PDF format. There is a minimal publication fee for authors who are members of Tsunami Society International for three years and slightly higher for non-members. Tsunami Society International members are notified by e-mail when a new issue is available. Permission to use figures, tables and brief excerpts from this journal in scientific and educational works is granted provided that the source is acknowledged.

Recent and all past journal issues are available at: http://www.TsunamiSociety.org CD-ROMs of past volumes may be purchased by contacting Tsunami Society International at postmaster@tsunamisociety.org Issues of the journal from 1982 thru 2005 are also available in PDF format at the Los Alamos National Laboratory Library http://epubs.lanl.gov/tsunami/

ISSN 8755-6839

SCIENCE OF **TSUNAMI HAZARDS**

Journal of Tsunami Society International

Volume 32 **Number 2** **2013**

IMPACT OF TSUNAMI FORCES ON STRUCTURES
The University of Ottawa Experience

D. Palermo, I. Nistor & T. Al-Faesly
University of Ottawa, Ottawa, Canada

A. Cornett
National Research Council, Ottawa, Canada

ABSTRACT

Over the past seven years, a comprehensive interdisciplinary research program has been conducted between researchers at the University of Ottawa and at the Canadian Hydraulics Centre (CHC) of the National Research Council of Canada. The objectives of this on-going research program are to identify and quantify forces that are imposed on near-shoreline structures when exposed to tsunami-induced hydraulic bores and to investigate mitigation strategies to dampen these forces. The experimental component of this research program involves two structural models (square and circular) that are tested in the High Discharge Flume at CHC. The structural models are instrumented to record base shear force-, base overturning moment-, pressure-, acceleration-, lateral displacement- and bore depth-time histories continually during testing. Impact loading resulting from wood debris of different sizes and located at pre-determined distances from the structural models is also studied. Furthermore, this research program aims to review tsunami-induced forces on structures prescribed by recent design documents.

Keywords: *Tsunami; hydrodynamic loading; debris impact; building performance; and design guidelines.*

1. INTRODUCTION

During the last decade, three significant tsunamis (Indian Ocean 2004, Chile 2010, and Japan 2011) have impacted coastal regions resulting in catastrophic human and economic losses. These events have illustrated that infrastructure located near coastlines in tsunami inundation zones is vulnerable to significant damage from rapidly advancing tsunami surges and bores. The tsunamis, while devastating, have provided the engineering community with unique opportunities to learn about the response of inland structures that are typically not designed to withstand the forces imposed by the resulting tsunami waves. They have provided an avenue to investigate the performance of non-engineered and engineered structures, and various building materials. In addition, beyond lateral loading, reconnaissance trips to the affected areas have brought to light other important structural mechanisms that need to be considered in the design of tsunami-resilient structures. These include, but are not limited to: debris impact loading and debris damming as a consequence of floating debris that is transported by the advancing tsunami flow; uplift forces associated with the rapidly rising water level; overturning of structures due to lateral loading; and scouring of foundations. The following provides specific details of the three major tsunamis mentioned above.

1.1 2004 Indian Ocean Tsunami

The 26 December 2004 Indian Ocean tsunami marks a significant historical event. Researchers and engineers became more attentive to tsunami hazard as a result of the significant damage to many coastal communities and the massive human casualties that was experienced across the Indian Ocean. Prior to this event, with the exception of a limited number of shelter-type structures, tsunamis were not considered in the design of inland structures located within inundation zones. It was also a "wake-up" call for other regions of the world located near subduction zones, particularly those located around the "Pacific Ring of Fire". The Indian Ocean tsunami was triggered by a 9.1 magnitude (Richter scale) earthquake along the northwestern coast of the Indonesian island of Sumatra. The earthquake focal depth for this event was approximately 30 km. The main fault rupture zone was approximately 90 km wide and 1200 km long. A maximum tsunami run-up of approximately 51 m was observed in Indonesia (NGDC, 2012). From a structural engineering perspective, significant lessons were learnt, such as the types of loading that are generated during a tsunami event and the vulnerability of non-engineered structures. Fig. 1 (a) highlights the global damage suffered by non-engineered residential structures due to the advancing tsunami flow. Figs. 1 (b) and (c) depict the large objects that were transported by the tsunami, which resulted in significant impact loading on structural components. Fig. 1 (d) captures the uplift and displacement of concrete dock slabs due to the rapidly rising tsunami.

Figure 1. Effects of 2004 Indian Ocean tsunami on structures (Saatcioglu et al., 2006a, 2006b): a) global damage to non-engineered concrete residential structure in Phuket Island, Thailand; b) debris impact and damming in Banda Aceh, Indonesia; c) debris impact from large vessels in Banda Aceh, Indonesia; and d) uplift of concrete slabs in Khao Lak, Thailand.

1.2 The 2010 Tsunami in Chile

On 27 March 2010, an 8.8 magnitude (Richter scale) earthquake struck offshore Chile, along the boundary between the Nazca and South American Plates. The earthquake focal depth for this event was approximately 30 km and was situated offshore Bio-Bio. Specifically, the epicenter was located 95 km NW of Chillan. *The rupture causing the earthquake had a width of over 100 km and a length of approximately 500 km and was parallel to the Chilean central coastline. The tsunami was first observed in Valparaiso 30 minutes after the earthquake (Dunbar et al. 2010). The highest wave height noted during a field survey by Lagos et al. (2010) was 11.2 m in the town of Constitución, while 8.6 m high waves were measured in Dichato and Tome. Fritz et al. (2011) noted that the tsunami reached a*

localized runup of 29 m on a coastal bluff at Constitución. The maximum inundation distance of approximately 1032 m was observed in Playa Purema. While many coastal communities suffered widespread damage, the number of casualties attributed to the tsunami was low. According to the International Tsunami Information Center, approximately 124 deaths were attributed to the tsunami. This was a direct result of two factors. First, Chile had experienced a major tsunami in 1960, which remains engrained in the memory of the local population. The 1960 event was triggered by a 9.5 magnitude earthquake, and approximately 1000 deaths were directly attributed to the tsunami. The highest wave height was 25 m at Isla Mocha (Dunbar et al. 2010). For the 2010 tsunami, in general, those living along the coast immediately searched for higher ground upon experiencing the ground shaking caused by the earthquake. Second, the central coastline of Chile is in close proximity to higher ground providing a natural vertical evacuation. Fig. 2 illustrates damage sustained by residential dwellings in the coastal community of Pelluhue. The photos reveal that the homes were fully inundated by the tsunami.

(a) (b) (c) (d)

Figure 2. Effects of 2010 Chile tsunami on residential structures in Pelluhue (Palermo et al., 2013): a) global damage to two storey-structure; b) punching failure of second storey masonry infill walls; c) damage to masonry infill walls and loss of load bearing elements at first storey level; and d) destruction of lower level columns.

The residential structure in Fig. 2 (a) suffered punching failure of the infill masonry walls at the second storey level and failure of the lower level bearing elements. Timber columns were used at the lower level as temporary vertical supports. The residence in Fig. 2 (c) also sustained complete failure of the lower level columns, and temporary timber columns were used to support the upper level.

Fig. 3 (a) shows signage that was evident in Tome to direct people away from the inundation area and to safe higher ground, while Fig. 3 (b) is a photo depicting the higher ground that is within the coastal region that is typical of many communities in Chile.

(a) *(b)*

Figure 3. Evacuation: a) tsunami evacuation route directions in Tome, Chile (Palermo et al., 2013); and b) higher ground in Pelluhue, Chile

1.3 2011 Japan Tsunami

A powerful earthquake of magnitude 9.0 (Richer scale) occurred at a depth of 30 km under the Pacific Ocean, near the northeast coast of Japan. The epicenter of the earthquake was located approximately 129 km east of Sendai, Honshu, and the subsequent tsunami arrived on the northeastern coast of Japan approximately 15 minutes thereafter, leaving little warning time for many villages and communities. Local run-up heights of up to 48 m were estimated (Chock et al. 2012). This event was responsible for approximately 15 867 deaths, 6 109 injuries, and 2 909 people missing. The Japanese Cabinet Office estimated direct losses of more than $309 billion due to damage to housing, roads, utilities, and businesses, making it the most expensive natural disaster on record. The destruction caused by this tsunami was surprising. Japan is a leading country when it comes to protection against tsunami; however, the tsunami waves displaced, overtopped and destroyed large structures, such as seawalls, which were initially constructed to mitigate the impact of tsunami waves on local communities. The designs of these structures were based on historical tsunamis and were not necessarily sufficient considering probabilistic-based tsunami events. Fig. 4 illustrates the effects of the tsunami, including breaching and overtopping of large concrete sea walls, floating vessels, overturning of a concrete building, and punching failure of a reinforced concrete wall panel.

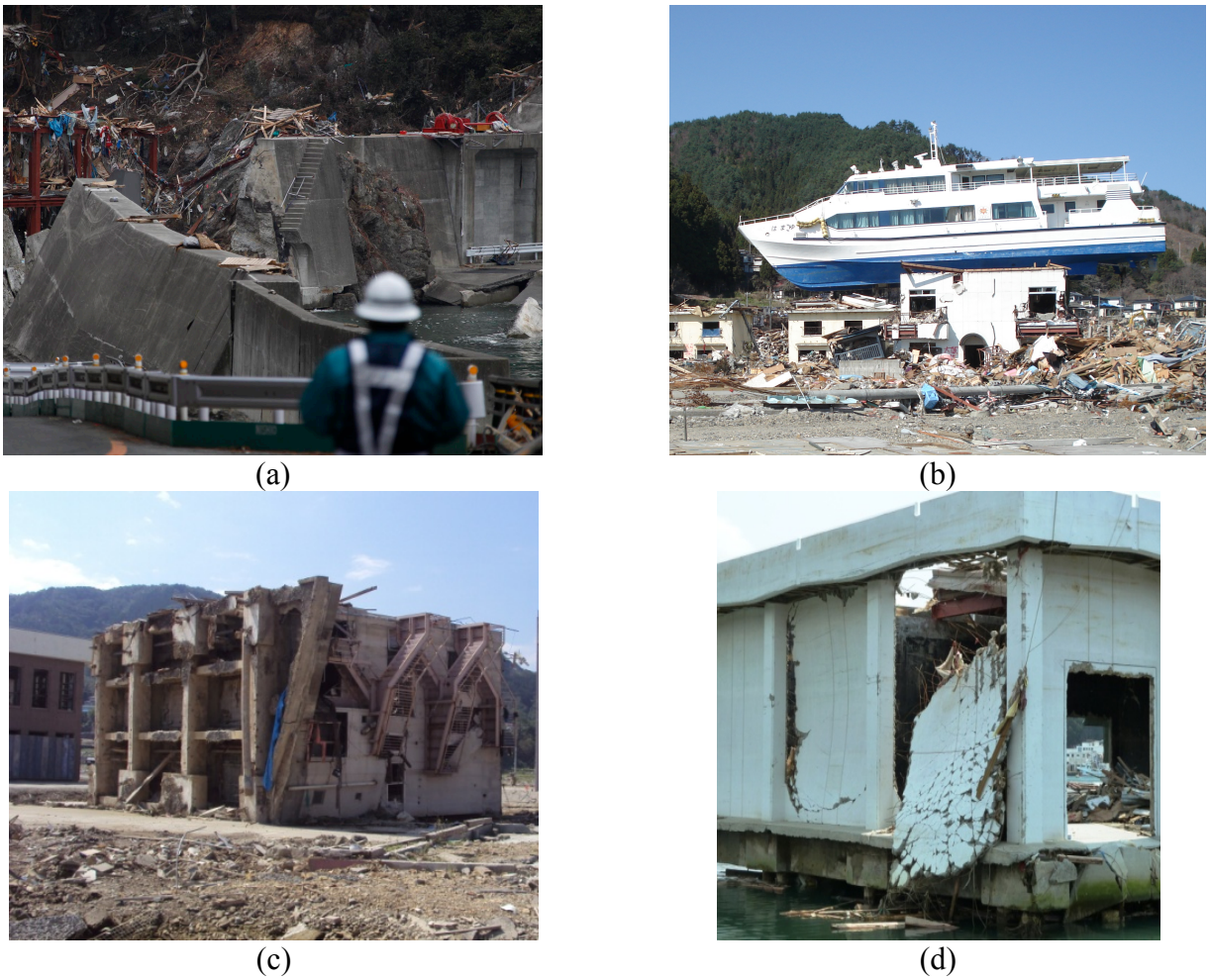

Figure 4. Effects of 2011 Japan tsunami on structures (Nistor, 2012): a) breaching and overtopping of concrete sea walls in Taro; b) impact loading from large vessel in Otsuchi; c) overturning of reinforced concrete apartment building in Onagawa; and d) punching failure of reinforced concrete walls in Onagawa

2. EXPERIMENTAL PROGRAM

In response to the observed structural damage of near-shoreline structures in tsunami inundation zones, an experimental testing program was developed between the University of Ottawa and the Canadian Hydraulics Centre (CHC) of the Natural Research Council (NRC) of Canada. The motivation for this research originated from findings of a field reconnaissance mission to Thailand, Indonesia and Sri Lanka following the 2004 Indian Ocean tsunami (Nistor et al., 2006). One of the main objectives of the program is to identify the forces imposed on structures from turbulent

hydraulic bores that are representative of the tsunami-induced bores generated in many of the areas affected by tsunami inundation during the 2004 Indian Ocean, 2010 Chile and 2011 Japan tsunamis. This was achieved by partitioning a pre-existing open channel high discharge flume at CHC and installing a swinging hinged gate. The gate was installed near the upstream end of a 1.3 m wide by 7.3 m long channel, and was capable of impounding water in the closed position. The gate is able to open rapidly, releasing a turbulent hydraulic bore that travels downstream and impacts structural models (Nouri et al., 2010). This mechanism is similar to a dam-break phenomenon. Chanson (2005) demonstrated that dam-break flows could provide a reasonable simulation of tsunami-induced turbulent hydraulic bores. Fig. 5 is a photo of the high discharge flume with the gate in the open position producing a turbulent hydraulic bore.

Figure 5. Turbulent hydraulic bore generated in the high discharge flume at the Canadian Hydraulics Centre

Fig. 6 provides top and elevation view drawings of the experimental setup wherein the location of the wave gauges used to measure the water depth; the structural models and mitigation walls are labeled. Also shown are the three impounded water levels investigated in this experimental program.

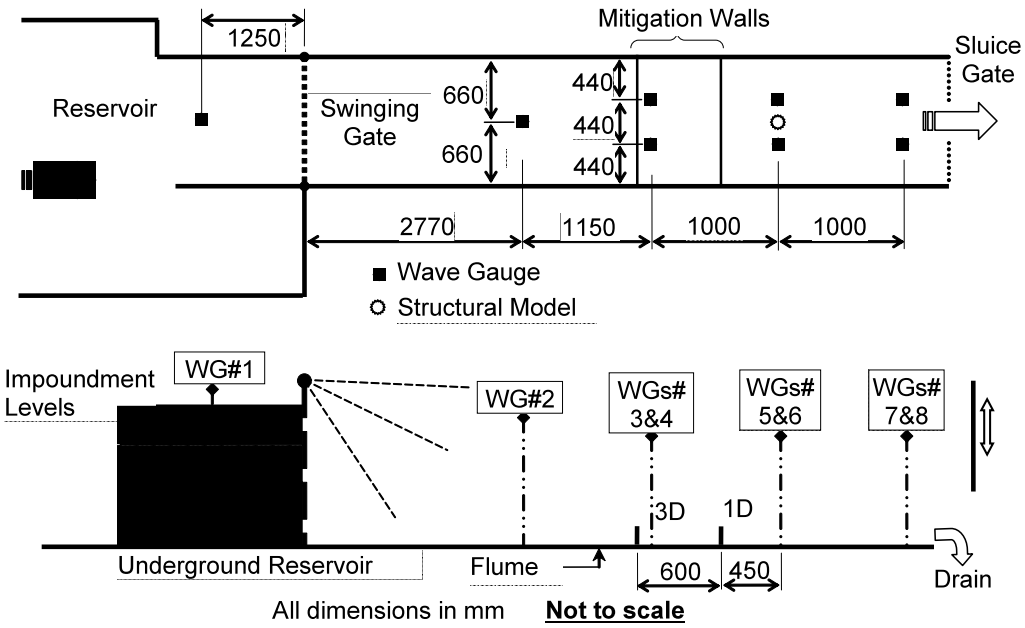

Figure 6. Drawings of experimental setup

Two hollow structural models, square and circular in cross section, were used in this experimental program. The hollow square structural model has 305 mm x 305 mm cross section, measured to the outside of the section. The walls are 6.35 mm thick and consist of acrylic glass sheets. The hollow circular model, also of acrylic material, has an outside diameter of 305 mm with a wall thickness of 9 mm. Photos of the two structural models installed in the flume are shown in Fig. 7.

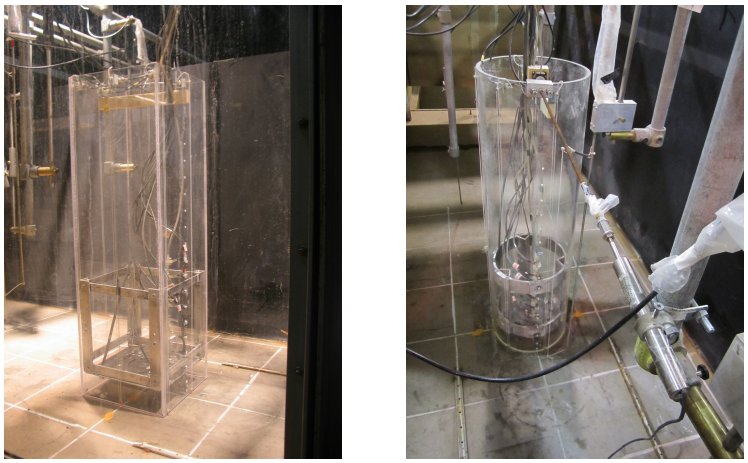

Figure 7. Hollow square and circular structural models (Al-Faesly et al., 2012)

The structural models were rigidly fastened to a six degree-of-freedom high-frequency dynamometer that, in turn, was fixed to the floor of the flume. The dynamometer was used to record base shear forces and base overturning moments. Ten pressure transducers were arranged vertically on the outer surface of the structural models to record pressures. Nine of the ten transducers were spaced at intervals of 50 mm starting from the flume floor, while the tenth transducer was positioned 20 mm above the flume floor. Pressures on different faces of the structural models were obtained by rotating the models. An accelerometer and a linear variable displacement transducer were placed at the top of the models to record accelerations and displacements in the direction of the flow, respectively. In addition to the instrumentation placed on the models, the flume was fitted with several capacitance water level gauges (Fig. 6) to record the water depth along the flume. All sensor measurements were recorded continuously during testing, at rates up to 1000 samples per second, to obtain time history responses.

A number of parameters and processes have been investigated in this experimental program, including: the water level impounded behind the swinging gate, the initial condition of the flume bed (dry or wet), the shape of the structural model impacted by the hydraulic bores, the response to debris impact, and the performance of upstream mitigation walls intended to reduce the peak forces acting on the structural models.

3. EXPERIMENTAL RESULTS

The experimental results presented herein include bore-depth time histories at the location of the structural model, base shear force-time histories in the direction of the flow recorded for the square structural model, and flow velocity-time histories at the location of the structural model. The bore depth and corresponding velocity provides essential data to evaluate current force expressions used in design documents.

3.1 Bore Depth, Base Shear Force, and Pressures

Fig. 8 provides typical bore depth-time history responses recorded by the water level gauges placed around the square model and the base shear force-time history recorded by the dynamometer. These results were generated with the 550 mm impounded water level behind the swinging gate in the closed position. The upstream gauges (WG9 and WG10) measured an instantaneous spike in water level followed by a sharp decrease. This spike coincided with the initial impact of the bore front on the structure and was caused by a thin jet of highly aerated water flowing rapidly up the column face. Immediately following the initial impact, some water was reflected upstream while the advancing bore was surging up the front face of the structural model. This led to a second rise in water level followed by a quasi-static flow condition where the water level remained approximately constant with time.

The base shear force-time history shown in Fig. 8 (b) also reveals an initial spike in force, which occurs when the leading edge of the turbulent bore impacts the structural model. Thereafter, there is a

drop in force as the bore rebounds upstream from the upstream face of the model. This is followed by an increase in force as the bore flow accumulates in front of the structure causing a "bulb-like" wake. The latter mechanism leads to the maximum force experienced by the structural model, and has been termed "run-up force" (Palermo et al., 2009) or "transient hydrodynamic force". The first impact or impulse force (approximately 222 N) was recorded when the water depth at the upstream face of the column (at gauge WG9) was approximately 0.52 m. The run-up force was approximately 264 N, which coincided with a water level of approximately 0.39 m. The force-time history does not suggest the presence of a steady hydrodynamic force; however, between 8 to 10 s, the force was approximately constant and equal to 220 N. The water level recorded at WG9 was approximately 0.36 m during this time period.

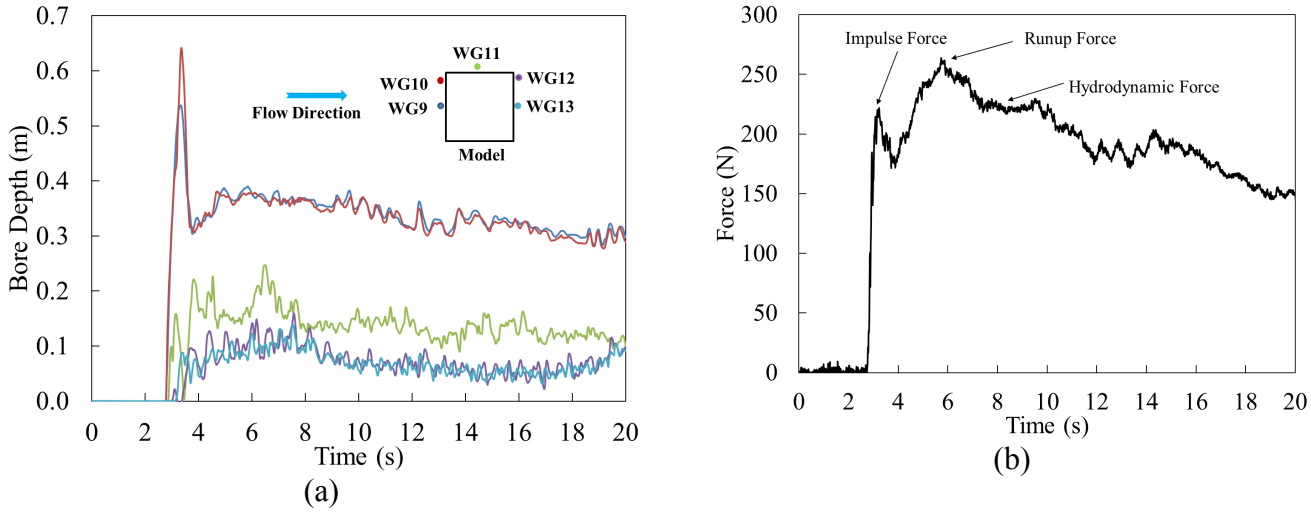

Figure 8. Experiment data for 550 mm impoundment depth: a) bore depth-time histories around the square model; and b) base shear force-time history

Fig. 9 provides still images from a video recording showing the three stages of flow interaction with the square structural model that coincide with the force components identified in Fig. 8 (b). The three stages are: the reflection of the flow from the front face of the square model after the initial impact; the run-up condition as the rebounding water meets with the advancing bore and surges up the model; and the quasi-steady state flow condition.

(a) (b) (c)

Figure 9. Hydraulic bore-structural model interaction: a) initial impact; b) run-up; and c) quasi-steady flow

Fig. 10 shows the vertical pressure distributions recorded on the upstream face of the square model at three different times during a single flow-structure interaction. The times correspond to the impulse force, run-up force and quasi-steady hydrodynamic force identified in Fig. 8 (b). For all three times, the pressure profiles were consistent with a hydrostatic distribution. Furthermore, it is evident that all pressure transducers, with the exception of the gauge located 450 mm above the flume bottom, which remained above the maximum water level, recorded pressures. Therefore, at all three times during the interaction, the water level on the upstream face of the square model reached approximately 400 mm. This result is inconsistent with the measurements at water level gauge WG9, and suggests that gauge WG9 recorded a higher water level during the initial impact as a result of the water rebounding off the upstream face of the structure. For the run-up and hydrodynamic force conditions, the pressure gauges recorded a slightly higher water level due to the water surging up the front face of the model.

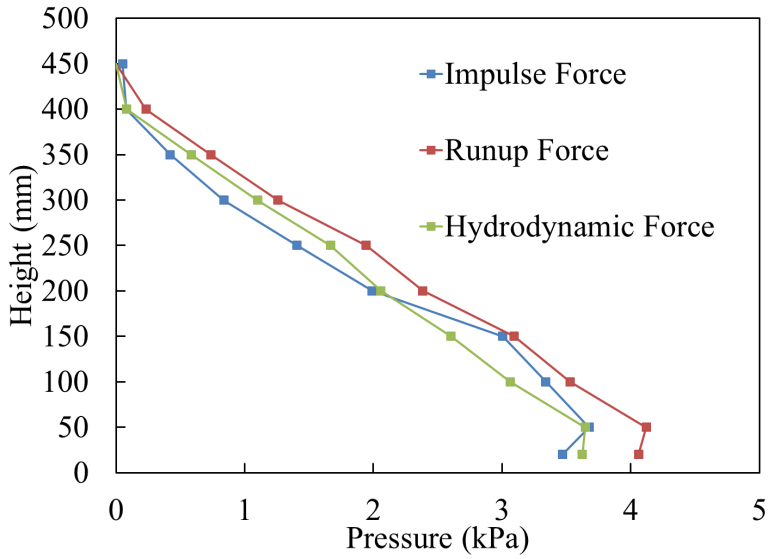

Figure 10. Vertical pressure distributions on the upstream face of the square model

From the hydrostatic pressure profiles of Fig. 10, the individual force components (i.e. impulse, run-up and hydrodynamic) can be evaluated. For each force component, the height of the pressure was assumed to be 400 mm, while the pressures at the base are approximately 3.67 kPa, 4.12 kPa, and 3.65 kPa, for the impulse, run-up, and hydrodynamic forces, respectively. These pressure values corresponded to the transducer readings 50 mm above the base of the structure. This slightly overestimates the pressure at the base of the structure, but offsets the 0 kPa pressures assumed at the 400 mm elevation. Based on these assumptions, the calculated forces were 224 N, 250 N, and 222 N for the impulse, run-up, and hydrodynamic force components, respectively. These are in close agreement with the base shear forces measured by the dynamometer and illustrated in Fig. 8 (b).

The bore depth measured at the location of the structure, without the structure in the flume, is shown in Fig. 11. For the 550 mm impoundment depth, the water reached a maximum elevation of 0.22 m at approximately 13.5 s. This peak water level was sustained for approximately 10 s as water drained from the impoundment. It is interesting to note that the water level on the upstream face of the structure was approximately 0.4 m based on the pressure readings. Therefore, the presence of the structural model causes a local increase in bore depth near the upstream face. In addition, the influence of the width of the flume relative to the width of the structural model may be a contributing factor.

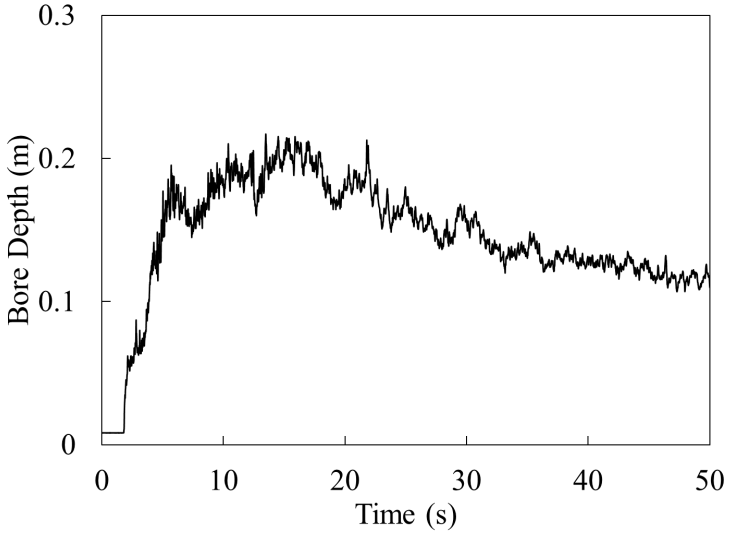

Figure 11. Bore depth-time history in the absence of the structural model

3.2 Bore Velocity and Hydrodynamic Forces

The bore velocity-time history corresponding to the measured bore depth-time history in Fig. 11 is shown in Fig. 12. The velocity was measured by seeding the water with 25 mm square paper beads and tracking their position by analysing images recorded by a high-speed video camera positioned above the flow. The video camera, as shown in Fig. 12 (a), was fastened 2.40 m above the floor of the flume at the location of the structure. Two wooden bar markers were arranged horizontally across the

width of the flume, 0.3 m apart from each other and 0.48 m above the floor of the flume. The distance (D_w) travelled by the paper, which was captured by the video camera, varied with the water depth and was adjusted according to the geometry shown in Fig. 12 (a). Therefore, using the adjusted distance and the time for the paper to flow between the wooden markers, the bore velocity-time history at the location of the structural models was calculated (see Fig. 12 (b)). Note that this procedure measures the velocity at the surface of the bore.

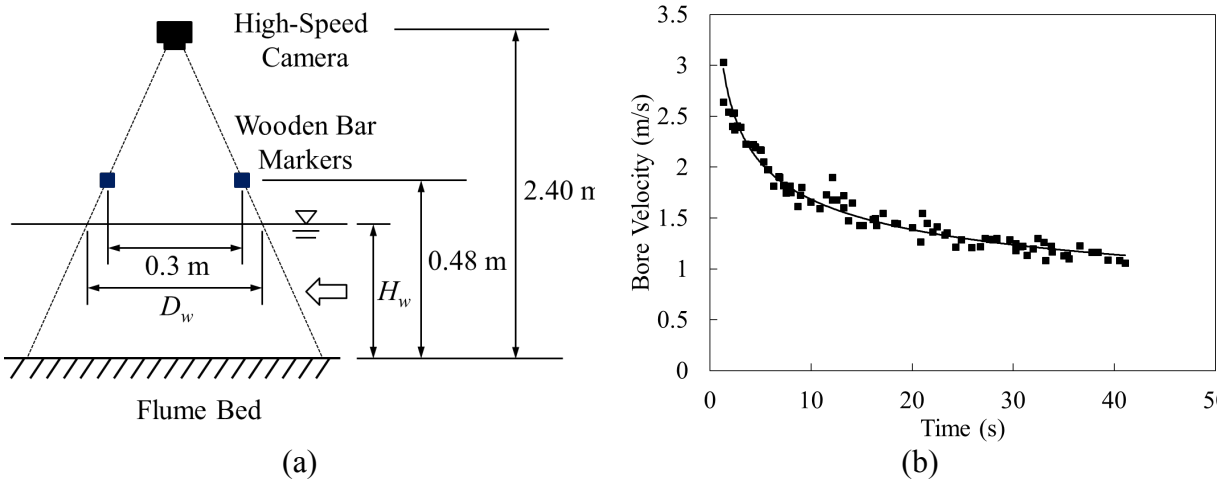

Figure 12. Bore velocity for 550 mm impoundment depth: a) velocity tracking setup; and b) measured bore velocity-time history at the location of the structural model

Fig. 12 clearly demonstrates that the bore front velocity was significantly higher than the velocity during the time period from 10 – 20 s in which the bore depth reached a maximum. The surface velocity near the leading edge of the bore was approximately 3.0 m/s, double the 1.5 m/s velocity that prevailed between 10 – 20 s. The bore depth-time history and corresponding bore velocity-time history were used to calculate the momentum flux (the product of the bore depth and the corresponding velocity squared). This parameter is used to estimate the hydrodynamic forces as provided in Eqn. 2.1 and published in FEMA P646 (2012):

$$Fd=12\rho sCdBhu2max \qquad (2.1)$$

where r_s is the fluid density, (approximately 990 kg/m^3 for this test program); C_d is the drag coefficient, assumed equal to 2 for square elements; B is the width of the element (0.305 m for the square structure); and $(hu^2)_{max}$ is the maximum momentum flux, which would need to be estimated from the bore depth- and bore velocity-time histories for the site, or obtained by some other means. Fig. 13 (a) provides the calculated momentum flux-time history, while Fig. 13 (b) shows the hydrodynamic force-time history obtained by applying Eqn. 2.1. The base shear force-time history recorded by the dynamometer is included in the figure for comparison. Note that the two force-time histories are offset for clarity.

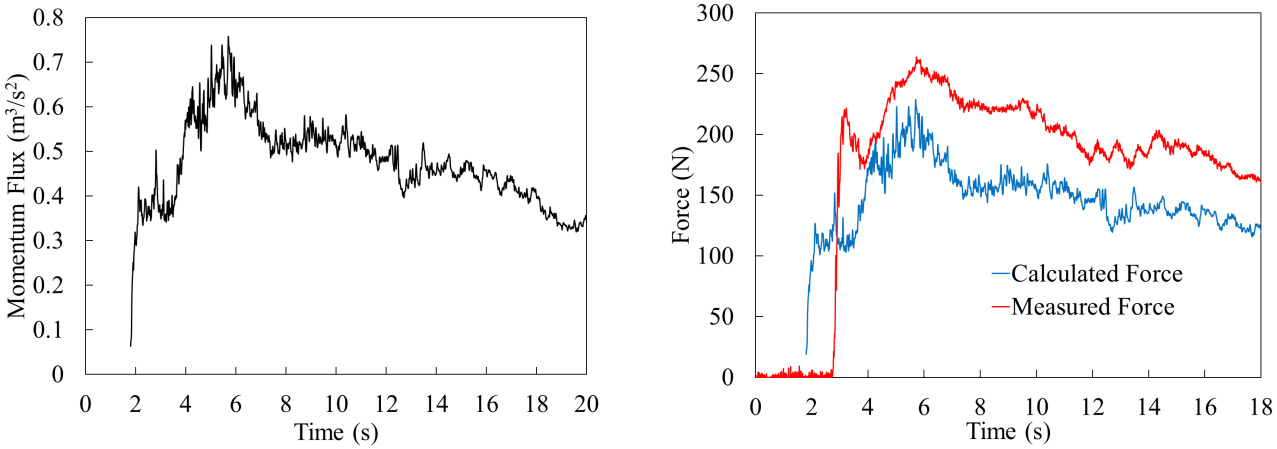

(a) (b)

Figure 13. Calculated values for 550 mm impoundment depth: a) momentum flux-time history; and b) base shear force-time histories

The results illustrate that the calculated forces follow the same trends as the measured forces; however, the calculated force under-estimates the maximum force in this case. The peak calculated force was approximately 229 N, while the peak recorded force was 264 N or 15% larger. This difference in peak force may be attributed to a number of sources, such as measurement error, variability between repeated tests, the confining effect of the flume walls, and error in the assumed value for C_d.

For a site where the bore depth- and bore velocity-time histories are not available, FEMA P646 provides an analytical approach to calculate the maximum momentum flux:

$$hu2max=gR20.125-0.235zR+0.11zR2 \quad (2.2)$$

where g is the acceleration due to gravity, R is the design run-up elevation, and z is the ground elevation at the base of the structure. For the experimental setup presented herein, z is taken as 0, and Eqn. 2.2 simplifies to:

$$hu2max=gR20.125 \quad (2.3)$$

FEMA P646 suggests that the design run-up elevation, R, be taken as 1.3 times the maximum run-up elevation to account for uncertainties in determining the design run-up. Using a maximum bore depth of 0.22 m from Fig. 11, and applying the 1.3 factor, Eqn. 2.3 predicts a maximum momentum flux of 0.098 m^3/s^2. The corresponding maximum hydrodynamic force using Eqn. 2.1 is 29 N. This result demonstrates that the momentum flux formulation (Eq. 2.2) provided in FEMA P646 may not be applicable for near-zero sloping beaches. Similar findings were obtained for a number of other similar tests conducted by the authors (Al-Faesly et al., 2012). Note that FEMA P646 (2012) indicates that Eq. 2.2 is based on one-dimensional nonlinear shallow water theory for a uniformly sloping beach.

3.3 Debris Impact Testing

The field surveys conducted after the 2004 Indian Ocean, 2010 Chile and 2011 Japan tsunamis highlighted the severe impact of debris on structures. As part of this experimental program, debris impact tests were conducted using 3 wood logs of different size and mass: 77 mm x 77 mm x 490 mm (1.09 kg), 77 mm x 77 mm x 916 mm (2.19 kg), and 77 mm x 154 mm x 490 mm (2.26 kg). Fig. 14 (a) shows the setup of a typical debris impact test prior to the opening of the gate, and Fig. 14 (b) captures the impact of the log against the circular structural model. The wooden logs were placed on the floor of the flume at pre-determined distances from the structural model before each test. As the bore advanced downstream from the gate, the flow accelerated and transported the debris, causing it to impact against the structural model.

(a) (b)

Figure 14. Debris impact testing: a) initial setup; and b) debris impacting circular structural model

Fig. 15 provides a typical impact test result for the circular structural model. The results correspond to the 1.09 kg wood debris initially located 1.75 m downstream from the swinging gate.

Fig 15 (a) provides the entire base shear force-time history where the spike in force is attributed to the wood log impacting the structural model. The first impact occurs shortly after the bore front reaches the upstream face of the model. The first impact force was approximately 279 N (net of the force imposed by the flow of the water) with a corresponding rise time of 0.005 s. Fig. 15 (c) shows the base shear force-time history between 3 and 4 s where two additional impacts are evident. They occur due to the log rebounding from the structure and then being carried back into the structure by the bore. The second and third net impact forces were approximately 220 N and 144 N, respectively, with rise times of 0.005 s and 0.007 s. Fig. 15 (b) demonstrates that the first impact was a direct longitudinal strike, while the second and third impacts were more of a transverse strike (Fig. 15 (d)). The second and third impact forces were smaller than the first impact force due, in part, to the reduced velocity of the log and the change in orientation from longitudinal to transverse.

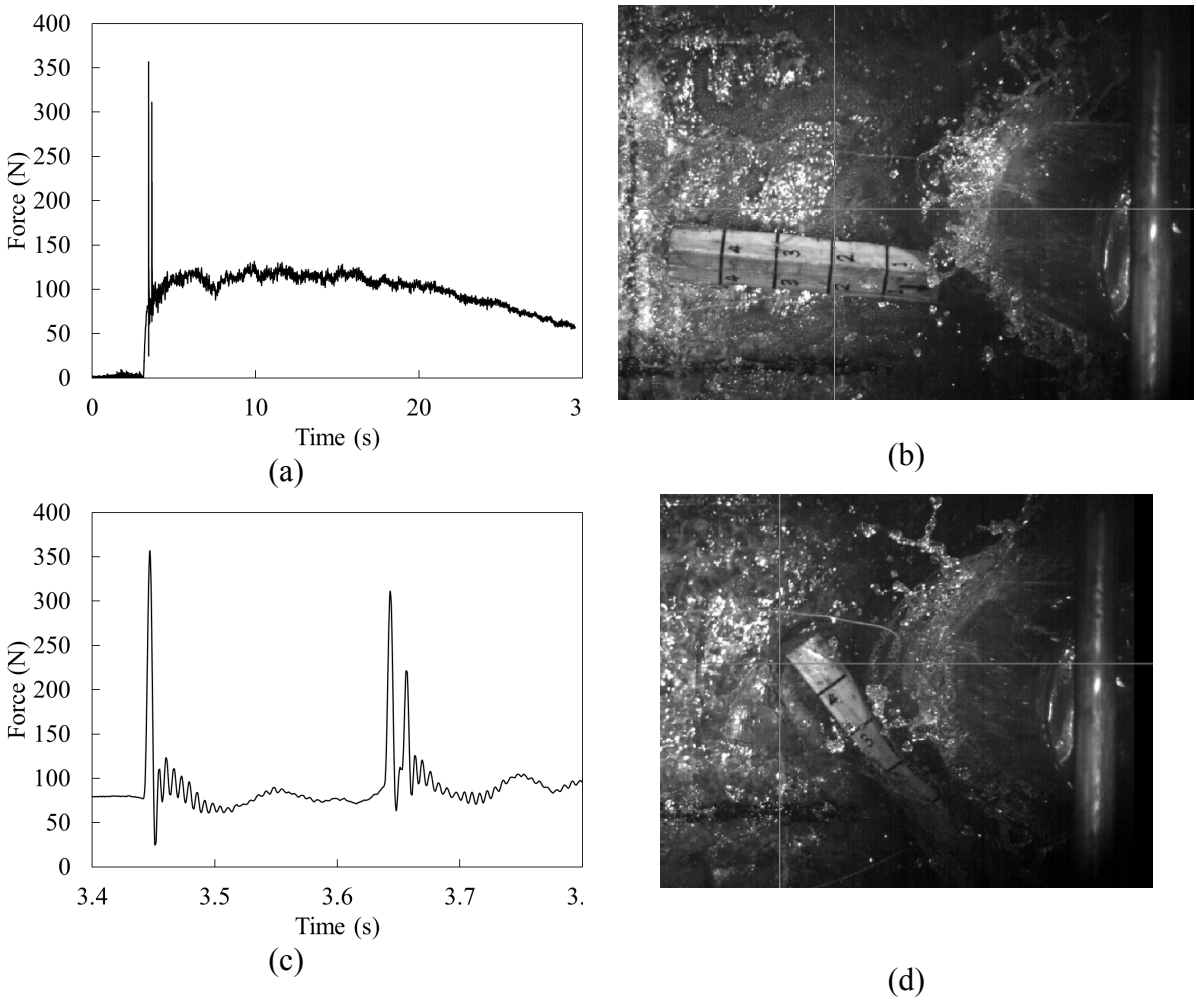

Figure 15. Debris impact test results: a) base shear force-time history; b) orientation of first impact; c) base shear force-time history of subsequent impacts; and d) orientation of subsequent impacts

3.4 Flume Bed Condition

Another interesting phenomenon observed during the experiments was the influence of the condition of the flume bed. Fig. 16 compares the base shear force-time histories experienced by the square structural model when subjected to flows generated by the 550 mm impoundment depth. Fig. 16 (a) illustrates the measured response under dry-bed conditions (an initial condition with negligible water on the flume bed), which typically corresponded to the first test of the day. This condition could reasonably represent in-land ground conditions during the arrival of the first tsunami wave. Fig. 16 (b) provides the measured response under wet-bed conditions (an initial condition wherein the flume bottom was covered by a thin film of water), which corresponded to all subsequent tests. This could be representative of the ground conditions for subsequent tsunami waves. The corresponding bore depth-time histories are also superimposed in Fig. 16.

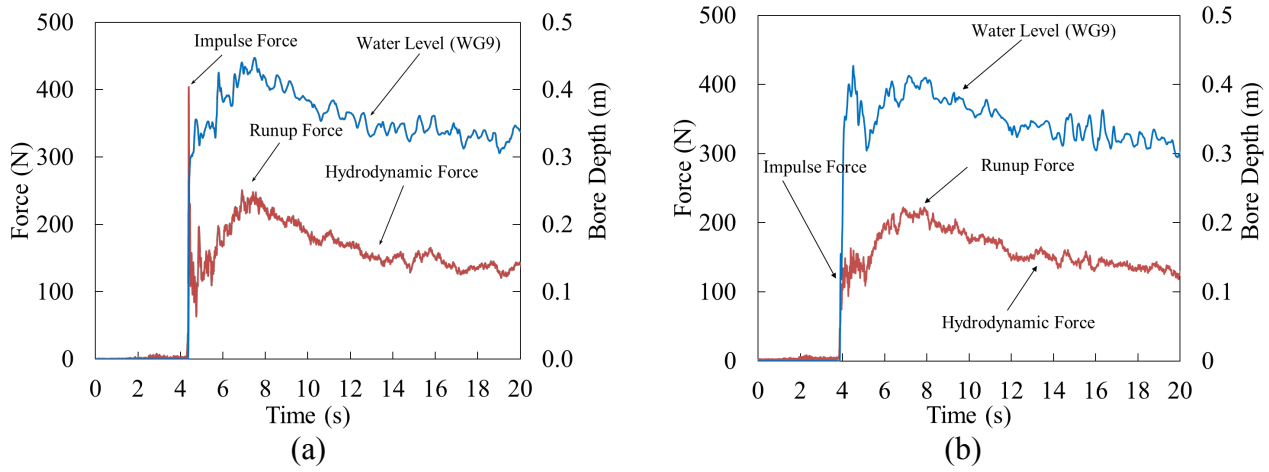

Figure 16. Effect of dry bed vs. wet bed for 550 mm impoundment water level: a) time histories for dry bed; and b) time histories for wet bed

The bore depth-time histories recorded by WG9, located near the upstream face of the structural model, for the wet- and dry-bed conditions are similar. The base shear force-time histories are also similar beyond the initial impulse force. The only notable difference is the initial impulse force. For the dry-bed condition, the initial impulse force was approximately 404 N, while under the wet-bed condition; the initial impulse force was only 134 N. It became evident from observing high-speed video recordings that the leading edge of the bore front was steeper in the case of the dry flume bed, which is attributable to the greater friction generated by the dry-bed surface. This phenomenon resulted in the significantly higher impulse force for the dry-bed condition.

4. CONCLUSIONS

The severe impact of tsunami-induced bores on near-shoreline structures has been well documented by recent events in the Indian Ocean (2004), Chile (2010), and Japan (2011). Based on observations from site visits to these areas, the University of Ottawa in collaboration with the National Research Council of Canada have collaborated to conduct experimental studies to further the knowledge of tsunami loading of near-shore structures. This paper has presented typical findings, from which a number of conclusions are drawn:

1. A dam-break process can be used to generate turbulent hydraulic bores similar to those observed in recent tsunami events.
2. The presence of a structure modifies the bore depth- and bore velocity-time histories around the structure relative to the undisturbed flows in the absence of the model.

3. Three distinct phases of forcing were typically observed during testing: impulse, run-up, and quasi-steady hydrodynamic.
4. For the test results presented herein, the vertical pressure distribution on the upstream face of a square structure can be well approximated as a hydrostatic pressure distribution throughout the flow-structure interaction.
5. Properly assessing the momentum flux is critical to accurately predicting the hydrodynamic force-time history. The analytical solution provided by FEMA P646 to calculate the maximum momentum flux is not applicable for near-zero sloping beaches.
6. Impact testing revels that single debris objects can generate multiple impact events, with the first impact generating the maximum force.
7. The initial dryness of the flume bed was found to have a strong influence on the magnitude of the initial impulse force, with significantly larger impulse forces recorded under a dry-bed condition.

REFERENCES

AL-FAESLY, T., PALERMO, D., NISTOR, I., AND CORNETT, A. (2012). Experimental modeling of extreme hydrodynamic forces on structural elements. *International Journal of Protective Structures (IJPS)*, **3:4**, 477-505.

CHANSON, H. (2005). Analytical solution of dam break wave with flow resistance. Application to tsunami. *31st International Association for Hydro-Environment Engineering and Research (IAHR) Congress*, 3341-3353.

CHOCK, G., ROBERTSON, I., KRIEBEL, D., FRANCIS, M., AND NISTOR, I. (2012). Tohoku Japan tsunami of March 11, 2011 – Performance of structures, *American Society of Civil Engineers (ASCE)*, 297 p.

DUNBAR, P., STROKER, K., AND MCCULLOUGH, H., (2010). Do the 2010 Haiti and Chile earthquakes and tsunamis indicate increasing trends? *Geomatics, Natural Hazards and Risk* **1:2**, 95-114.

FEMA. 2012. Federal Emergency Management Agency P646, Guidelines for Design of Structures for Vertical Evacuation from Tsunamis, Washington, D.C., USA.

FRITZ, H. M., PETROFF, C. M., CATALÁN, P. A., CIENFUEGOS, R., AND WINCKLER, P. (2011). Field survey of the 27 February 2010 Chile tsunami. *Pure and Applied Geophysics* **168:11**, 1989-2010.

LAGOS, M., ARCAS, D., RAMIREZ, T., SEVERINO, R., AND GARCIA, C. (2010). Alturas de tsunami modelas y observadas. Evento del 27 de Febrero de 2010. Chile/Resultados Preliminares.

NISTOR, I. (2012). Field survey of the tsunami impact and loading on structures – Engineering lessons of the 2011 Tohoku Tsunami. *4th International Conference on Protection of Structures against Hazards*.

NISTOR, I., MURTY, T., NIRUPAMA, N., JINSONG, X. (2006). Some physical oceanographic processes in the behavior of the 26th December 2004 tsunami. *15th Congress of the Asia-Pacific Division of IAHR and International Symposium on Maritime Hydraulics, IAHR*, 81-90.

NGDC. (2012). National Geophysical Data Center, National Oceanic and Atmospheric Admisnitration. http://www.ngdc.noaa.gov/hazard/recenttsunamis.shtml.

NOURI, Y., NISTOR, I., PALERMO, D., AND CORNETT, A. (2010). Experimental investigation of tsunami impact on free standing structures. *Coastal Engineering Journal, World Scientific* **52:1**, 43-70.

PALERMO, D., NISTOR, I., SAATCIOGLU, M., AND GHOBARAH, A. (2013). Impact and damage to structures during the 27 February 2010 Chile tsunami. *Canadian Journal of Civil Engineering*, doi.org/10.1139/cjce-2012-0553.

PALERMO, D., NISTOR, I., NOURI, Y., AND CORNETT, A. (2009). Tsunami loading of near-shoreline structures: A primer. *Canadian Journal of Civil Engineering* **36:11**, 1804-1815.

SAATCIOGLU, M., GHOBARAH, A., AND NISTOR, I. (2006A). Performance of structures in Thailand during the 2004 Sumatra earthquake and tsunami. *Earthquake Spectra,* Earthquake Engineering Research Institute, **22:S3**, 355-376.

SAATCIOGLU, M., GHOBARAH, A., AND NISTOR, I. (2006B). Performance of structures in Indonesia during the 2004 Sumatra earthquake and tsunami. *Earthquake Spectra*, Earthquake Engineering Research Institute, **22:S3**, 295-320.

ISSN 8755-6839

SCIENCE OF **TSUNAMI HAZARDS**

Journal of Tsunami Society International

Volume 32 **Number 2** **2013**

METHOD FOR EVALUATING VULNERABILITY TO TSUNAMIS OF LOW-TO-MEDIUM INTENSITY: APPLICATION TO THE FRENCH CÔTE D'AZUR

M. Terrier, D. Monfort, J. Lambert, S. Le Roy, R. Pedreros & O. Sedan

Bureau de Recherche Géologique et Minières, Orléans, France

ABSTRACT

Today, the study of tsunami risk has become a recurrent concern for crowded coastal areas, and this is true even for those that normally seem to be the least prone to the phenomenon. In this framework, the BRGM has for the past five years been compiling and managing an historical database devoted to tsunamis that may have affected the shores of France. Concurrently, simulations of tsunamis for plausible major seismic or gravity-driven events have been conducted. These have indicated that the south of France is indeed subject to the risk of a tsunami of low to medium intensity. Between 2009 and 2010, the research project RATCOM has made it possible to establish the principles for assessing vulnerability and calculating damage and human losses for moderate tsunamis. The method thus developed is complementary to those already proposed for tsunamis of larger intensity. Applications of this method using the BRICE (©brgm) simulation tool for risk scenarios reveal that the level of risk has increased quite substantially over just a few decades, even for tsunamis of low to medium intensity (water height less than 1 m). This is essentially due to the exponential growth of urban development along the coastline and to tourist pressure. Although such events will not cause destructions to buildings comparable to those in Indonesia (2004) and Japan (2011), still weak phenomena can be responsible for serious human losses. On the Côte d□Azur, the potential number of victims is large enough to warrant immediately instating preparatory measures designed to cope with the possibility of such a scenario.

Keywords: *tsunami, base de données, simulation, dommages, France*

Vol. 32, No. 2, page 77 (2013)

1. INTRODUCTION

Understanding the risk presupposes assessing the tsunami hazard (endangered zone, intensity of the phenomenon/probability of occurrence). It also presupposes an assessing the vulnerability of stakes with respect to tsunamis. Assessing the tsunami hazard for a region relies on two main components: a solid knowledge of past events and the simulation of tsunamigenic events. An interpretation of these data should make it possible to identify the zones most liable to risk as well as the corresponding level of intensity. Knowledge of past events involves studies of paleo-tsunamis (geological and/or archeological observations, over time intervals that may span several thousand years) and mining archives (intervals generally covering a few centuries, or more rarely Antiquity). The simulation of tsunamigenic events concerns not only plausible fictitious events, but also modeling actual ones in the past. In this latter case, it will be necessary to confront the output of models with information on the most reliable historical tsunamis. A synthesis of all this information (archives, simulations) then allows a hazard assessment to be performed.

In the wake of the catastrophic December 2004 tsunami in the Indian Ocean, a considerable amount of work was accomplished with the purpose of improving our understanding of structural and human vulnerability to tsunamis. On the basis of damage curves in structures versus the tsunami's intensity, the methods developed follow an approach that is comparable to the ones called on in seismic vulnerability and risk assessments, such as those implemented under HAZUS (FEMA, 2004) or Risk-UE (Lagomarsino *et al.*, 2006; Giovinazzi, 2005). These methods, being intended for strong-intensity tsunamis, do not allow risk to be calculated for low or medium intensity ones, that is, those characterized by energies too low inflict major structural damage, but high enough to result in human losses. Between 2009 and 2010, the research project RATCOM has made it possible to define, for moderate tsunamis, the principles for assessing vulnerability and calculating damage and human losses. Concurrently, with support from UNESCO, a CENtre d'Alerte aux Tsunamis, CENALT, has been set up. Its role is to monitor strong earthquakes that occur in the western Mediterranean and in the northeastern Atlantic. As to France, the Direction générale de la sécurité civile (DGSC, the directorate-general for civil security) depending on the Ministry of the Interior was assigned the coordination of the ALDES project concerning the descending part of the tsunami alert system. In this framework, several tsunami scenarios with implementation of the assessment method developed in the RATCOM project were carried out along segments of France's southern coast.

Work conducted by the BRGM over recent years, particularly for France□s Mediterranean shore, is integrated in the overall chain of assessment and management of tsunami risk, including: the establishment of a database containing historical events, the regional identification of tsunamigenic sources and simulation of plausible major tsunamis, the proposal of a method for assessing damage and losses for low to medium intensity tsunamis and its application for the purposes of local management of the risk.

2. RESEARCH ON TSUNAMIS THAT MAY HAVE REACHED THE SHORES OF FRANCE

2.1. Working method

Research on historical tsunamis that may have affected French coasts (continental France, Reunion Island, the Antilles, New Caledonia), undertaken since 2005, consists in:

- seeking out and acquiring original documentary sources, in manuscript or printed form, that are the most contemporary with the event: these are the so-called "primary sources";
- covering a very wide scope of investigations, documents sourced in France and elsewhere, and of different sorts: books, scientific and historical articles, manuscripts, newspapers, travel journals, chronicles, earthquake catalogues, etc.;
- simultaneously, looking for weather data: strong storms affecting the coasts of metropolitan France or offshore, hurricanes and cyclones in the French islands of the Indian Ocean, the Pacific Ocean and the Caribbean Sea;
- if feasible (i.e., subject to the quality of data), analyzing and interpreting the physical characteristics and calibrating these phenomena according to the Ambraseys-Sieberg scale (six degrees of increasing intensity);
- seeking to determine the cause of the event: earthquake, ground movement, underwater explosion, volcanic eruption, meteorite, seiche, meteorological depression, or still unknown.

Concerning events for which the documentary description leaves no doubt as to the tsunamigenic nature of the phenomenon (movements of ebb and flow of the water, retreat of the sea followed by inundation in a specific space-time frame, etc.), each event is described by a series of parameters characterizing the tsunamigenic wave at the location where the tsunami was observed. As of today, the catalogue references 80 events (Lambert and Terrier, 2011) structured in a database accessible on the web at www.tsunamis.fr.

2.2. Catalogue of tsunamis identified along the French Mediterranean coastline

The origins of a majority of the tsunamis observed along the French Mediterranean coastline are still uncertain. Some submarine landslides, however, have been clearly identified, such as that of Nice in 1979 or the one at Antibes and Villefranche-sur-Mer in 1564, this latter having been triggered by an earthquake, the epicenter of which (Intensity VIII MSK) was situated 40 km inland. Other tsunamis on the Mediterranean coast are indisputably of seismic origin, like that of 1887, widely felt across the Côte d□Azur, or those in 1819 and 1831 that seem to have been limited to the immediate vicinity of French shores (San Remo).

3. SIMULATION OF TSUNAMI SCENARIOS CONCERNING THE FRENCH MEDITERRANEAN COAST

Together with the catalogue of historical tsunamis, the simulation of historical or fictitious tsunamigenic events is an essential prerequisite to assessing the hazard. Indeed, applying scenarios

selected for their enhanced impact with respect to the coasts considered, the simulations allow general elements to be obtained as to the potential level of exposure of the coasts and to estimate the incidence and form that the tsunamis might take on reaching the shore. This is the framework in which several scenarios have been proposed. This portion of the work consisted in: 1) the characterization of tsunamigenic sources for the French Mediterranean coast; 2) the preparation of several bathymetric grids at various scales, adapted to near-and far-field tsunamis; 3) the choice and simulation of reference events; 4) the preparation of maps indicating the highest water levels and arrival times on the shore for each scenario.

3.1. Tsunamigenic sources of seismic origin

Because mapping and characterizing active faults of all the western Mediterranean Sea are not possible with the current level of knowledge, the identification phase for tsunamigenic sources of seismic origin necessarily had to be based on seismic zonation. For this purpose, different sources of geological (geological maps of Europe and seismotectonic ones of the Mediterraneean Basin, as well as other publications), bathymetric and seismological data were collected and interpreted. These gave rise to a deterministic seismic zonation for the Western Mediterranean (Fig. 1). The zonation obtained (Terrier, 2007) describes for each seismic zone: 1) the main tectonic and seismic characteristics with, as appropriate, the return period for very strong earthquakes; 2) the largest earthquake, either recorded or mentioned in the archives; 3) the parameters of the maximum earthquake selected (magnitude, fault plane rupture dimensions, fault slip...).

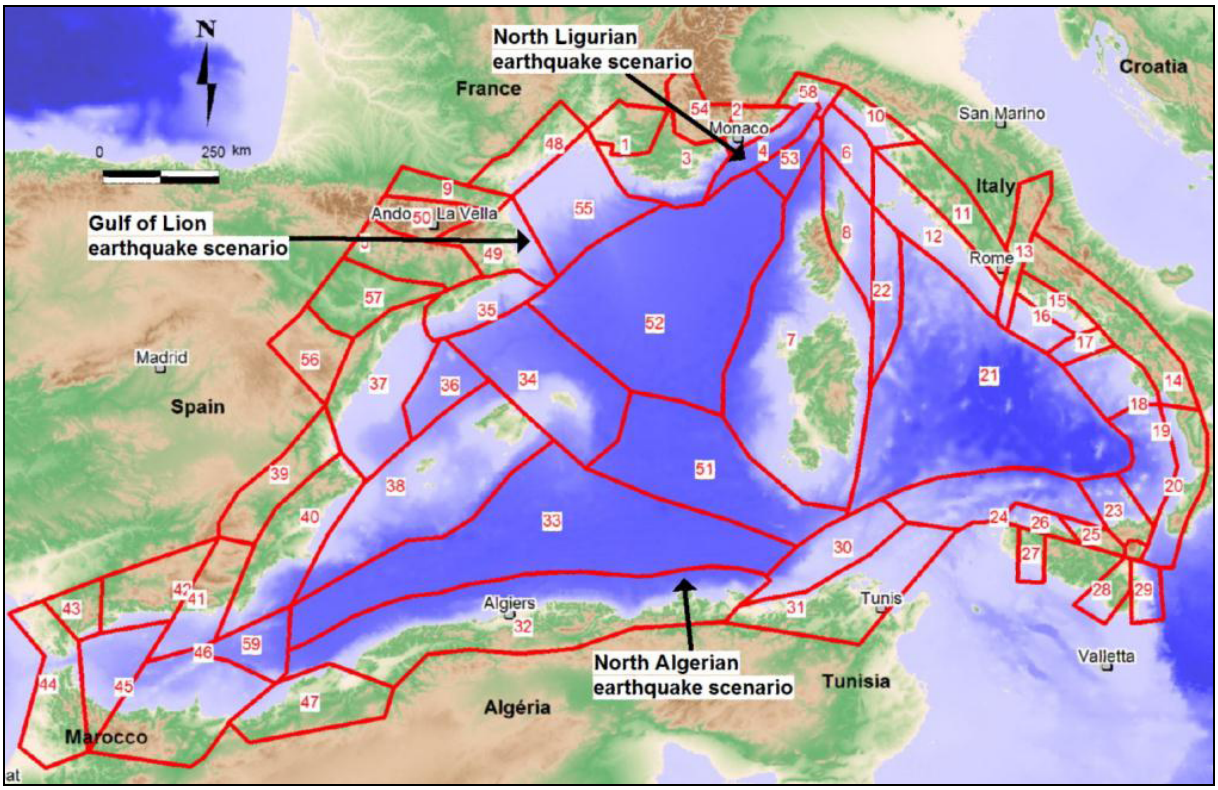

Figure 1 - Seismic zonation and choice of scenarios for seismic sources used in the study of tsunami risk along the French Mediterranean coastline (Terrier, 2007).

3.2. Tsunamigenic sources of submarine landslide origin

Offshore of the French Mediterranean coast, the morphology of the maritime zone is highly irregular morphology, locally featuring steep slopes. It furthermore may be overlain by formations that are relatively thick and poorly consolidated. Thus these zones are conducive to submarine landslides. Based on bathymetric data, as well as knowledge of submarine sedimentary bodies, and supported by known gravity-driven events, fossil or modern-day, a zoning of submarine gravity-driven movements on the continental shelf and foot-slope off the French Mediterranean shores was assigned to IFREMER (Cattaneo, 2007), Fig. 2. Each of these zones is characterized by a typical slide of maximum volume for a return period ranging between several centuries and several millennia. Each typical slide is described by the following parameters: length, width, maximum thickness, mean slope, mean depth, the nature of the destabilized sediments, "SLUMP" or "SLIDE", "RUNOUT" and direction of propagation. Details about the zoning and how it was achieved are given in Cattaneo (2007).

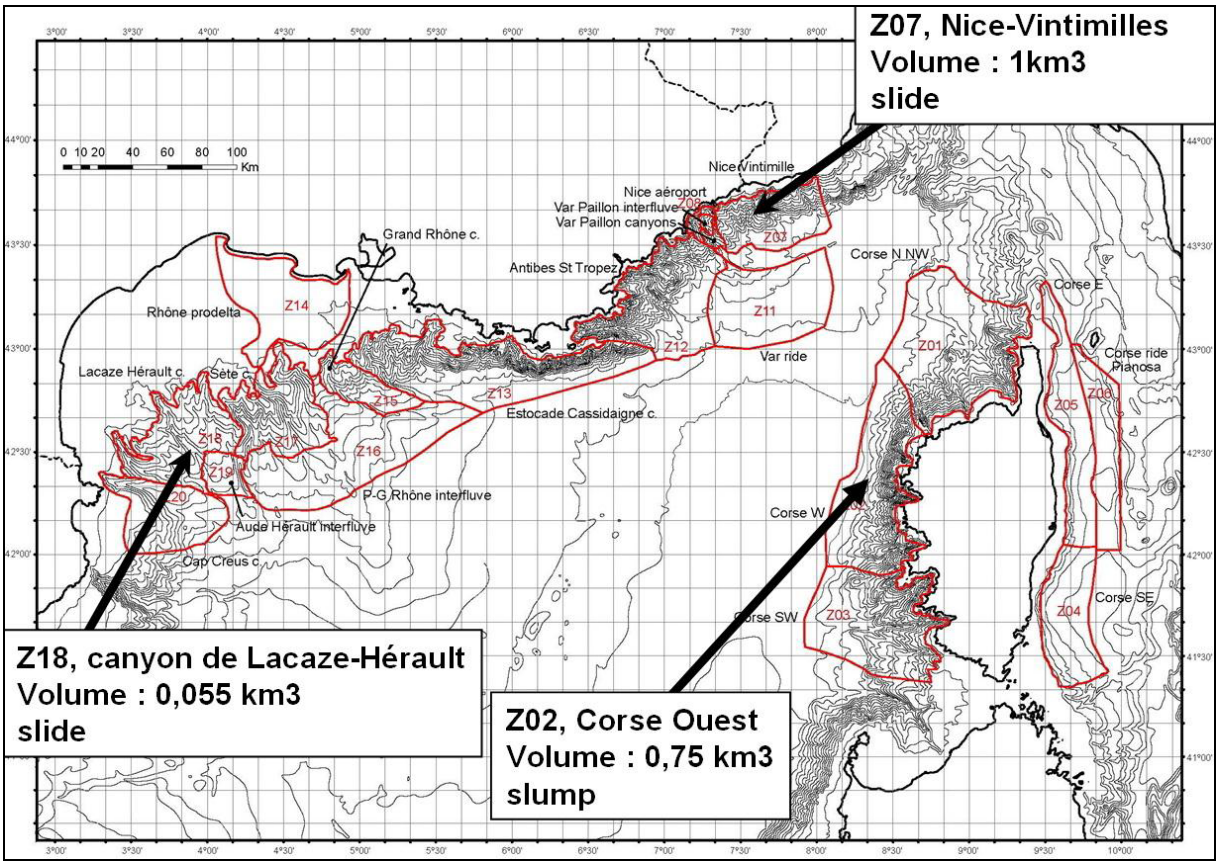

Figure 2 - Zoning of submarine landslides and choice of scenarios for the study of tsunami risk along the French Mediterranean coast (Cattaneo, 2007).

3.3. Simulations of plausible major events

More than twenty simulations performed on low-resolution grids (meshes ranging from 2250 m to 750 m per side) were initially performed. These concern either historical events or fictitious ones.

These preliminary calculations allowed the choice of six reference scenarios (Fig. 1 and 2) to be oriented more judiciously, and calculations with a finer mesh were conducted for these. The events involved are maximum plausible ones with return periods ranging from several centuries to a few millennia. The results obtained (Pedreros and Poisson, 2007; Terrier *et al*., 2007) demonstrate that France□s Mediterranean coast is not exempt from tsunamis (Table 1). This said, the expected intensity remains relatively moderate.

Table 1 - A summary of the results of the tsunami scenarios (Terrier *et al.*, 2007).

Scenarios :	Simulation with Magnitude or volume	Maximum amplitude wave calculated near the shore (at 10m depth)	Arrival time calculated	Part of the French coast reached (amplitude > 0.5m)
North Ligurian earthquake	M = 6 ,8	2m at Antibes	10□ to 15□	St Tropez to Nice
North Algerian continental margin earthquake	M = 7,8	4m at St-Tropez, Cannes 3m at La Ciotat, Nice, Villefranche	95□ to 100□	Marseille to Menton
Gulf of Lion earthquake	M = 6,7	0.6m at Agde, Port-la-Nouvelle	60□ to 80□	Between Perpignan and Béziers
Landslide of the west continental Corse margin	V =0,75 km3	5m to 6 m to the North of Porto	5□ to 15□	South-West shore between Porto and Bastia
Landslide of Lacaze-Hérault canyon	V=0,055 km3	1.5m at Perpignan 1m at Frontignan and Beauduc	45□ to 80□	Perpignan to Beauduc
Landslide of Nice-Vintimille continental margin	V = 1 km3	4m at Antibes 3m at Nice	10□ to 20□	St-Tropez to Menton (until San Remo, Italia)

4. ASSESSING DAMAGE AND LOSSES FOR TSUNAMIS OF WEAK TO INTERMEDIATE INTENSITY

For the French Mediterranean coastline, the analysis of historical tsunamis and simulations of major tsunamigenic events indicate a maximum water-level height of less than 4 m. The tsunamis concerned are accordingly of low to medium intensity, i.e., their degree is less than 4 on the Sieberg scale modified by Ambraseys (1962) or than intensity VI on the Papadopoulos and Fokaefs scale (2005). Between 2009 and 2010, the research project RATCOM has made it possible to define, for moderate tsunamis, the principles for assessing vulnerability and calculating damage and human losses for moderate tsunamis (Monfort et al., 2010). The method developed in this study is complementary to those already proposed for tsunamis of higher intensity. It enables us to obtain a quantitative estimate of damages to individuals and property for different levels of aggression (tsunami scenario), bearing in mind that: 1) The hazard predicted for the French

Mediterranean coastline is weak to intermediate, with run-up that does not exceed 3 m; 2) The stakes most exposed there are port areas (the most severely impacted by historical tsunamis) and the population (the recent, postwar tourist phenomenon); 3) In light of the context, and according to the type of structure, this can act as a "shelter." The following methodological steps are distinguished: choosing and mapping the stakes, assessing their vulnerability, simulating the tsunami and evaluating losses.

4.1. Choosing and mapping the stakes

The choice of stakes takes into account an analysis of feedback from intermediate-intensity tsunamis as well as the socio-economic context (very high population density during tourist seasons). The stakes considered are:

- Population density for each quarter and for different times of year (winter, summer) and of day (night, afternoon), using data on Ponchettes beach in Nice (Robert et al., 2008) as a reference. The breakdown into quarters takes into account the type of building encountered, the nature of land-use (beach, commercial zone, etc.) and topography. Each geographic entity is considered to be uniform with respect to the three aforementioned criteria.
- Camp grounds.
- Underground car parks (number of levels and parking spots).
- Marinas and fishing harbors (number of moorage slips).
- Communication lines (highways and railways).
- Seaside buildings (their footprint and structural type). The structure□s typology takes into account openings at ground level, the number of stories and the presence of a basement. A distinction is made between light structures (beach huts, for example) and heavy, reinforced constructions.

The characterization of the stakes is defined on the basis of a survey in the field and consultation of regional authorities and tourist bureaus. It is completed by a thorough-going analysis of aerial photos for a range of dates (boundaries of the quarters, distribution of structures and, as appropriate, a mean indication of the level of occupation of the beaches via a head count).

4.2. Assessing the vulnerability of the stakes

4.2.1. Population situated outdoors

Assessing human vulnerability depends schematically on how capable individuals are of protecting themselves (notably through their ability to move around) or withstanding an inundation. Flooding may be characterized according to various physical factors such as duration of submergence, run-up, the current□s direction and speed, and the solid load that is transported. Koshimura et al. (2006) propose limits beyond which the danger level is significant, with a risk of drowning, that is, a restricted capacity of mobility, calculated in terms of the run-up and current speed. The results in Koshimura et al. are globally coherent with those that have been selected by the French authorities in the framework of the elaboration of Plans de Préventions des Risques aux Inondations (flood risk prevention plans). In the context of RATCOM, the aggression component is expressed by the value couple "maximum flood level /maximum speed" at a given moment, Fig. 3. Thanks to this limit, it is possible to identify, over the time the inundation will last, those areas

where people will be able or not to withstand the flow on their own. This curve, however, does not factor in the transport of heavy and/or voluminous debris, which are liable to further hinder the mobility of persons.

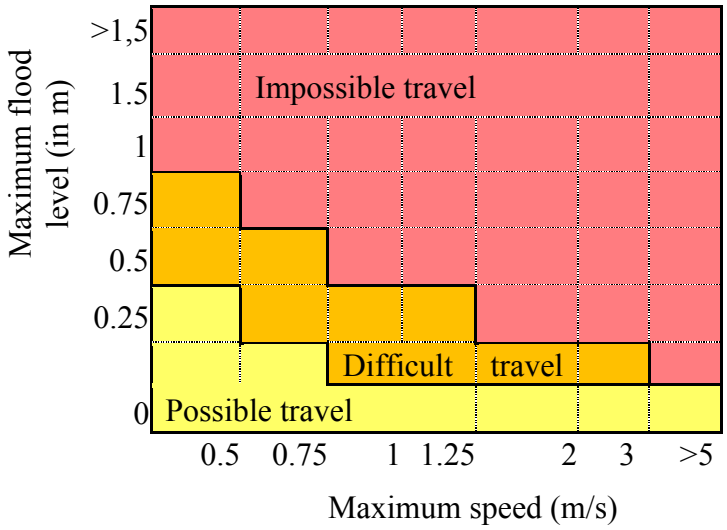

Figure 3 - Limit to the ability to move used in the framework of the RATCOM project.

Based on analyses of feedback from catastrophic tsunamigenic events, Guha-Sapir (2006) and Nishikiori et al. (2007) observed mortality rates of between 6% and 10% within a population of individuals swept away by the current. Following the 2011 tsunami in eastern Japan, Mimura et al. (2011) calculated a mortality rate ranging between 3.3% and 15% according to location. Based on this work, for an affected population unable to move and situated outdoors, a mortality rate of 10% was determined.

4.2.1 Population situated indoors

The analysis of feedback from historical and modern-day events shows that, except in the case of a tsunami generated by a nearby earthquake (with strongly felt vibrations), in all other instances it is preferable to be inside (excluding basements) than out. The approach for assessing the vulnerability of persons situated inside buildings and subject to the tsunami aggression alone follows the four following steps:

1) Typology of the structure with respect to the number of stories and the transparency of the ground floor (Fig.4) :

   - Type 1. A multi-story building surmounting a transparent ground floor (presence of shops, picture windows...) which allow water to enter the ground floor easily.
   - Type 2. A multi-story building surmounting a closed ground floor, that is, with walls that protect against the wave impact.
   - Type 3. A transparent one-story building (ground floor).
   - Type 4. A one-story building (ground floor) with walls that protect against the wave impact.

Maximum flood level (in m)									
	H >1,5	2	2	2	2	2	2	2	2
	1 to 1.5	2	2	2	2	2	2	2	2
	0.5 to 1	1	2	2	2	2	2	2	2
	H < 0,5	1	1	1	1	2	2	2	2
Building of type 1 or 3 Open ground floor		< 0.5	0.5 to 0.75	0.75 to 1	1 to 1.25	1.25 to 2	2 to 3	3 to 5	> 5
		Maximum speed (m/s)							

Maximum flood level (in m)									
	H >1,5	2	2	2	2	2	2	2	2
	1 to 1.5	1	1	1	1	1	2	2	2
	0.5 to 1	1	1	1	1	1	2	2	2
	H < 0,5	1	1	1	1	1	1	1	1
Building of type 2 Close ground floor, and several storied building		< 0.5	0.5 to 0.75	0.75 to 1	1 to 1.25	1.25 to 2	2 to 3	3 to 5	> 5
		Maximum speed (m/s)							

Maximum flood level (in m)									
	H >1,5	2	2	2	2	2	2	2	2
	1 to 1.5	1.5	1.5	1.5	1.5	1.5	2	2	2
	0.5 to 1	1	1.5	1.5	1.5	1.5	2	2	2
	H < 0,5	1	1	1.5	1.5	1.5	1.5	1.5	2
Building of type 4 Closed ground floor, and single storey building		< 0.5	0.5 to 0.75	0.75 to 1	1 to 1.25	1.25 to 2	2 to 3	3 to 5	> 5
		Maximum speed (m/s)							

Figure 4 - Matrixes for exposure to tsunamis versus structural type.

2) Mapping the structure (location, footprint and structural type).
3) For each type of structure, an exposure matrix is defined (Fig. 4). Based on work by Kelman (2002) and the values considered in the framework of the "Plans de Prévention des Risques" for France, several levels of exposure have been distinguished. These depend on the maximum speed of flow and the maximum run-up:

- Level 0, building not flooded.
- Level 1, building flooded, people on the ground floor not swept away. Those on the ground floor feel the effects of the wave but can move around. In the case of multi-story building, these individuals can take shelter in the upper levels.
- Level 1.5, single-level building protected by an outside wall, flooded. People can move around but will have nowhere to take shelter.
- Level 2, building flooded, people on the ground floor are swept away or trapped. Those on the ground floor are carried off by the waves or drowned. In the case of a multi-story building, people in the higher levels will remain protected. Certain parts of the building may be damaged.

For a population trapped on the ground floor of buildings exposed to level 2 conditions, based on work by Guha-Sapir (2006), a 4% mortality rate is obtained.

Underground levels (cellars and car parks) constitute a specific type. The risk is considered to be level 2 once flooding reaches them.

For aggressions higher than those appertaining to levels 0 to 2, the behavior of the structure can be estimated using vulnerability curves derived from observations of the 2004 Indian Ocean tsunami or those proposed by Guillande et al. (2009), Garcin et al. (2007), Peiris (2006), and Léone et al. (2006).

4.3. The vulnerability of port areas

During a moderate-level tsunami, boats moored in ports number among the property incurring the severest damage. In the Mediterranean, where tides are weak, boats are moored with little slack. In the event of a sudden and strong variation in sea level, docking lines, quickly over-stretched, break, allowing the boats to float free. These will then crash into each other, toss up against port facilities or hit bottom. The variations in level due to the ebb and flow generate strong currents in ports. As to the methodology implemented, the aggression is expressed in terms of a variation in water level (Table 2). The damage estimate is based on analyses of feedback from events occurred in the Mediterranean, like the tsunami owed to the Boumerdès earthquake (2003) or the seiche („eigen oscillation□), from 2006 in the Balearic Islands than caused damages in the harbour zones comparable to those of the tsunami. As a rule, damage to small crafts (fishing boats or yachts) is far more extensive than for large ships. For small boats, the risk to those on board will be directly linked to that of the boat itself.

Table 2 - Risk assessment for ports and harbor areas.

Water level variation into the port	**Damage level**	**Damage ratio for ships**
< 0.5 m	Acceptable	
0.5 - 2 m	Some ships are damaged. Damages to mobile facilities from the harbor.	Between 10 and 20% (situation of Boumerdès in Menorca or Théoule-sur-Mer, Port Salis in Antibes 1979)
> 2 m, strong currents	High risk to break the moorings. High risk of damages to ships and boats. Damages to some fixed facilities of the harbour.	Situation after seiche event in 2006 in Ciutadella (Menorca)
Harbor dried, big waves above the embankment	Boats and ships hit the bottom. High damage ratio for the ships and facilities.	

5. APPLICATION TO A 1979-TYPE TSUNAMI SCENARIO IN NICE (FRANCE)

The vulnerability assessment method was tested via an application on the Côte d□Azur (southern France), using an event of the Nice 1979 landslide type and four time scenarios: mid-January 2012 at 2 a.m. and 3 p.m. and mid-August 2012 at 2 a.m. and 3 p.m. The landslide parameters chosen for the simulation (Table 3) are drawn from work by Silva Jacinto and Meyniel (2010).

Table 3 - Parameters determined to describe the Nice airport landslide for modelling the tsunamigenic source.

Parameters	**Considered values**
Coordinates (WGS 84) of the initial gravity center	N 43°38'44.4" E 007°12'55.0"
Coordinates (Lambert 3, m) of the initial gravity center)	X= 993 360 Y= 161 180
Direction of the landslide (referenced to the North)	182.3°
Depth	47 m
Slope from the landslide	1.,2°
Maximal length of the landslide	900 m
Maximal width of the landslide	700 m
Maximal thickness of the landslide	50 m
Density from slipped material	1.4

The numerical simulation of the tsunami□s generation and propagation was performed using the GEOWAVE software (Watts *et al.,* 2003). Subsequently, to model the submergence on land in an urban context (taking into account structures and coastal installations), a coupling was established between the GEOWAVE and SURFWB programs (Marche *et al.*, 2007). As to the bathymetric and topographical data used, these allowed three interconnected calculation grids to be implemented, with a resolution that increased between the foot slope and the shoreline (pixels at 45 m, 15 m and 4 m). The contour and elevation of the built environment and coastal installations drawn from the "building footprint" layer of the BDTopo (topographic database) of the Institut Géographique National (France□s national geographic institute) were superimposed on the digital elevation model. Details about the simulations are given in Le Roy *et al.* (2011).

5.1. Simulation of the tsunami

The maximum heights of the free surface reached during the entire 20-minute interval that was simulated indicate the significant size the tsunami probably attained in Antibes (Fig. 5).

Submergence was computed on a grid with meshes measuring 3.75 by 3.75 m. It indicates that the arrival on the coast of the first wave seems to have caused most of the flooding, with subsequent waves simply reinforcing it, and this with generally lower current speeds. Maximum run-up averages 1 to 2.5 m and, very locally, even 4 to 5 m (Fig. 6). As to the maximum run-up distance (inland from the coastline), the simulation yields 150 to 200 m in the northern portion of the area studied, about 100 m on the wide beach to the north-west (i.e., reaching the buildings), some 60 m at the beach next to the port of La Salis (or slightly more when the water succeeded in spilling over into the streets, and on the order of 110 m in the port of La Salis itself. The outlines of the flooded areas obtained by simulation are fairly compatible with those reported by witnesses (Sahal and Lemahieu, 2010).

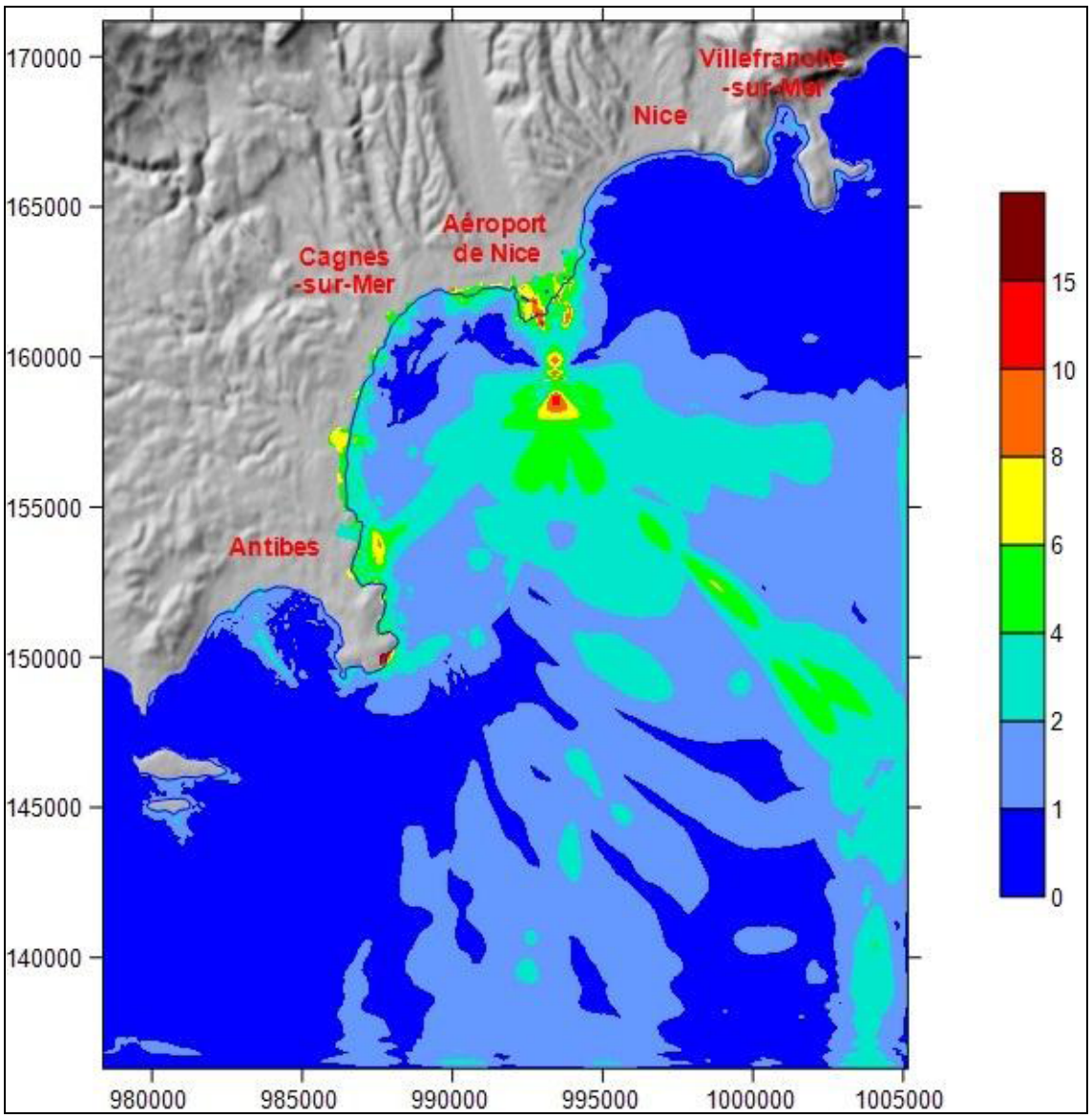

Figure 5 - Simulation of the Nice 1979-type tsunami: maximum elevation (in m) de highest water level.

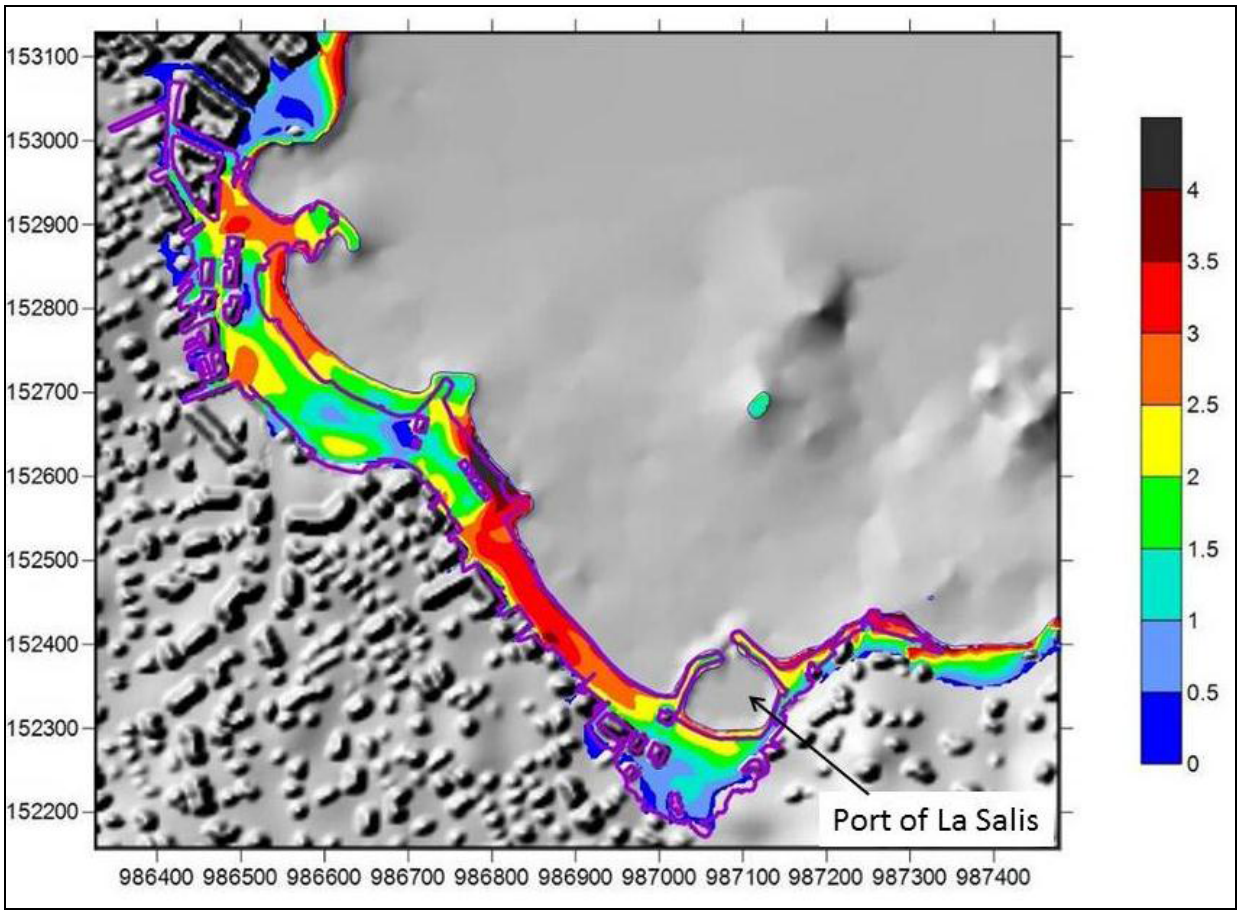

Figure 6 - Simulation of the Nice 1979-type tsunami : maximum run-up heights on land (in meters) and the flooded area identified by Sahal and Lemahieu (2010), in purple.

The simulation indicates furthermore that at the port of La Salis, the arrival of the tsunami results in a slight hollow a little over 5 minutes after the airport landslide (less than 5 cm, undetectable by witnesses), cf. Fig. 7. A wave almost 1.5 m high then penetrated the port some 6 minutes after the slide. The water in the port seems to have had difficulties in flowing out again. This can be explained by the fact that the port□s dikes had been largely submerged (the run-up height of the water being on the order of 0.80 m), hence the immediate filling of the basin, whereas once the sea had ebbed, it took much longer for the basin to empty again by overflowing the dikes or via the breach. The maximum level of water in the port was attained after some 11mn40 s., with a water-level increase of 2.5 m.

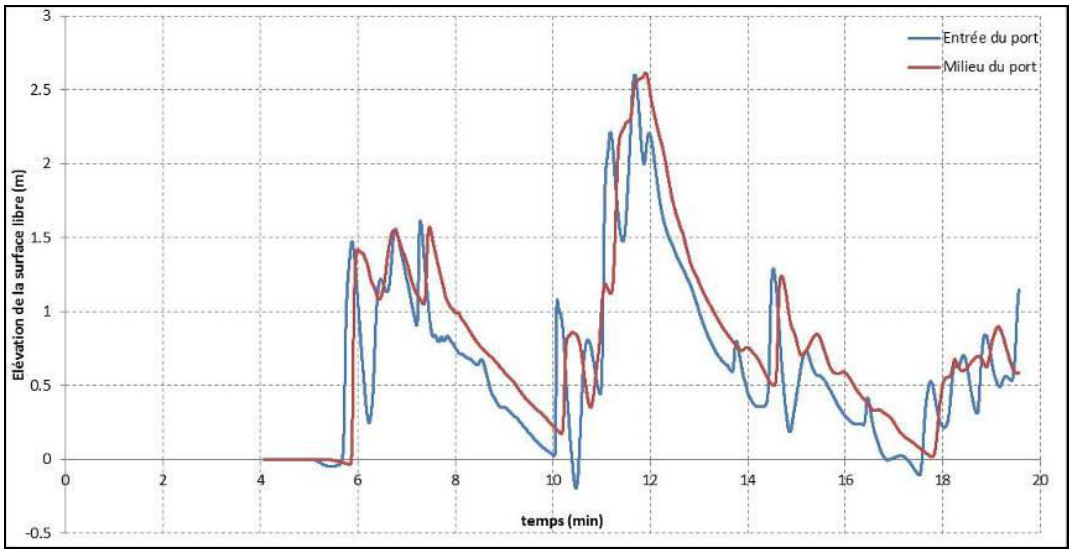

Figure 7 - Simulation of a Nice 1979-type tsunami: elevation of the free surface in the port of La Salis.

The maximum simulated speeds reached by the ebb and flow (norm and direction) very generally indicate values exceeding 3 m/s near the shore (Fig. 8). The analysis of the simulation film shows that the highest speeds were reached during the flow (the wave arrival) phase.

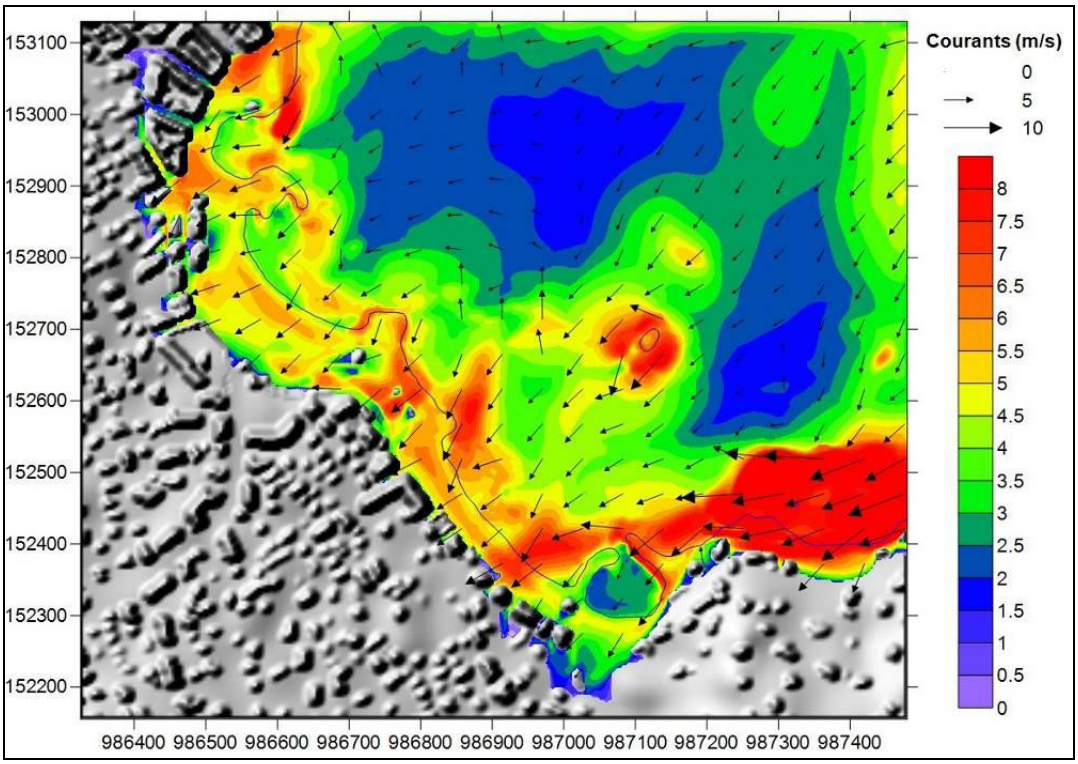

Figure 8 - Simulation of a Nice 1979-type tsunami: Maximum speeds attained by the currents: norms (in m/s) and directions.

5.2. Damage assessment

In 1979, the area most severely impacted by the tsunami was the shore of Antibes, with the death of one individual caught in the basement of his house located near the La Salis beach. In the same part of Antibes, the wave had flooded a street and borne away a dozen cars. The local newspaper reported some one hundred buildings affected by the surge, as well as thirty or so people injured. This event took place on October 16th in the early afternoon..

Using the results of the simulation of the 1979-type tsunami, a damage calculation was performed following vulnerability assessment principles described above and using the BRICE@brgm risk scenario simulation tool (Sedan, 2012). The scenario took into account the current distribution and typology of the built environment, as well as the population density off-season and during tourist season, nowadays situation.

5.2.1. Damage to the built environment

The analysis of the tsunami's impact on buildings does not depend on the season of the year or the time of day when the tsunami arrives. It indicates (Fig. 9), for the 68 buildings affected by the

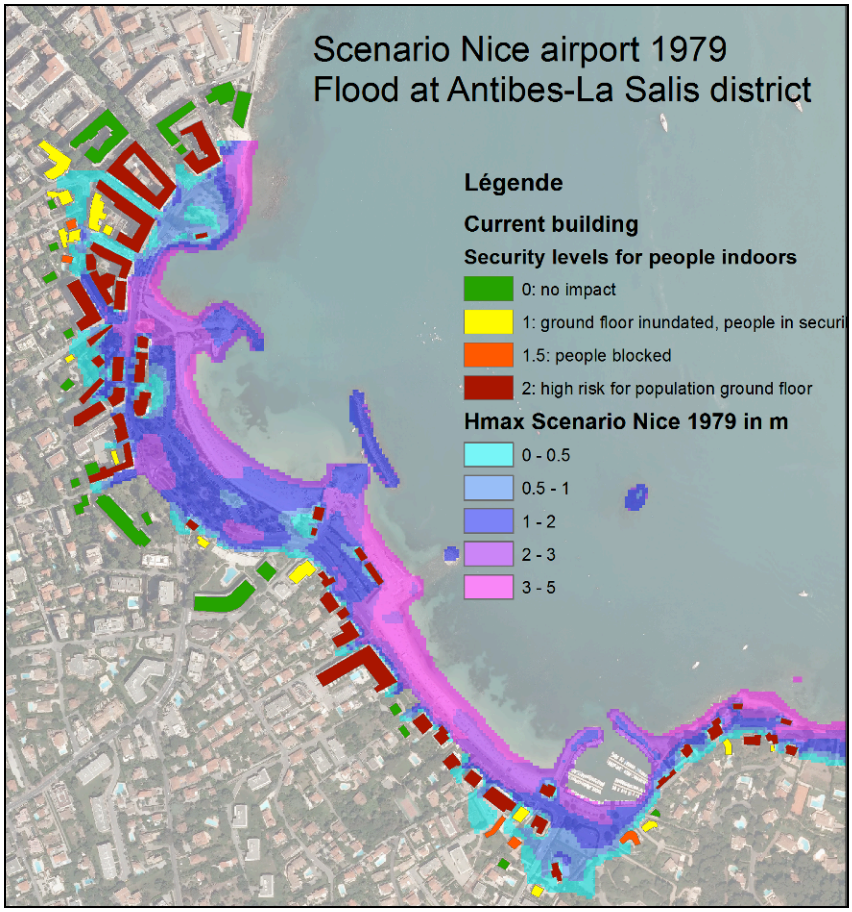

Figure 9 - Exposure levels for buildings in the La Salis quarter (Antibes) obtained with the Nice 1979 scenario.

inundation, that 25 would undergo a run-up height exceeding 0.75 m, 34 would be subjected to a current speed of over 1.5 m/s and 42 would present an exposure level of 2 (impossibility for persons inside to escape). This large number of building affected can be explained by the type of buildings with transparent ground floors which are frequently encountered by the shore.

As to masonry (reinforced concrete) structures impacted, the damage expected would be very minor. Damage would essentially be associated with the impact of the wave and of floating objects against the most fragile portions of the ground floor (windows, doors, picture windows and garden walls). With these water levels, only the lightest-weight structures would incur serious damage, such as the facilities of beach operators.

5.2.2. Human losses

An estimation of human losses takes into account the season (summer or winter) and the time of day. The simulation yields run-up heights exceeding 1.5 m and current speeds above 1 m/s for the La Salis quarter. With such a level of aggression, people are unable to withstand the flood. This estimate does not take into account fore-warning or the securing of people on the beach prior to the arrival of the flood. The inundation of the La Salis quarter affects the beaches, walkways, car parks and the busiest adjacent streets.

The number of individuals outside the affected buildings would amount to: 1) 2000 to 4000 people on August 15th in mid-afternoon and 2) 60 to 80 people on January 15th in mid-afternoon.

The mean estimate of the number of persons situated on the ground floor when the event occurs depends on the mean level of occupation of the buildings, according to the season, but also the time of day. Based on the mean occupancy rates proposed for earthquake scenarios (Coburn *et al.*, 2002), mean occupations of 45% in the mid-afternoon and 80% at night have been selected. As to the individuals situated inside the buildings, 42 buildings are considered to present an exposure level of 2. The number of people impacted for a mid-August scenario is at least ten times smaller than that of persons outside: nearly 200 in the middle of the afternoon and 300 at night. However, in winter, the number of persons impacted (between 90 and 150) is higher than that outdoors.

5.2.3. Damage in ports

Antibes has several marinas and harbors for fishing boats, totaling about 3000 berths, and an occupation rate in excess of 90%, whatever the season. The assessment for a 1979-type scenario would indicate damage to 8.5% of the boats. The most heavily damaged port would be that of La Salis, with a risk of crafts being stranded (thus with a strong likelihood of damage) in the neighborhood of 50% of the total present.

5.3.4. Scenario results extended to several municipalities

The scenario extended to several municipalities in the bay of Nice indicates that if an event similar to that of 1979 were to occur at the height of the tourist season (busiest peak in mid-August, mid-day), the tsunami could impact several thousand people. However, the interval when the beaches are crowded is estimated at 7% of the total time in a year. Generally speaking, the application of this risk-assessment method to an event-based scenario like that of the Nice airport in 1979 allows the following conclusions to be drawn:

- During a summer day, for the bay of Nice, several thousand individuals could be victims of the tsunami (including several dozen fatalities).
- Few urban sectors would be flooded by the event. Only light-weight structures (beach-side straw huts, structures made of wood, sheet metal and with large windows) would be severely damaged. The other buildings (masonry, reinforced concrete), particularly those with one or more stories, represent a risk-reduction factor for the population inside them.
- Ports are the infrastructures most prone to damage by tsunamis. Results indicate that several hundred boats could suffer from this type of event. More precise information concerning the seasonal occupation of each port would enable these estimates to be refined.
- The quality of results on damage assessments depends not only on a knowledge of the stakes and of vulnerability functions, but also on indications concerning flooding (height/speed) caused by the tsunami.

6. CONCLUSIONS

Historical studies indicate that the French Mediterranean coast has, on several occasions, undergone tsunamis of low to medium intensity. Today, seasonal crowding on the coast results in a level of risk that can be high during certain times of the year. The method currently implemented takes into account the fact that: 1) the built environment can be a risk-reduction factor for people under certain conditions (height and speed of the inundation, building typology, situation of the population when the event occurs) and 2) low to medium intensity tsunamis can cause substantial human losses. Beside exposure of the population, the method also addresses other stakes such as ports, seaside facilities (car parks, camp grounds and highways) and the built environment. In view of the complexity and diversity of the different parameters required to assess damage from tsunamis, it is difficult today to assign an approximate level to the margin of uncertainty inherent to the results obtained. To ensure better credibility to the method that has been developed, and subsequently to the results it produces, the development of the method should be pursued though dedicated research.

ACKNOWLEDGEMENTS

The authors wish to thank the French Ministry for the Environment and the Ministry of the Interior, for their contributions to funding the projects Tsunami.fr and ALDES, and the Ministry of the Economy and Finance as well as the Ministry for Research and Education for their contributions to funding the project RATCOM.

REFERENCES

AMBRASEYS N-N.,1962. Data for the investigation of the seismic sea-waves in the eastern Mediterranean. *Bulletin of the Seismological Society of America,* 52, 1962, 895-913.

BRGM/TSUNAMIS.FR : catalogue of the tsunamis observed in France, *http://www.tsunamis.fr*

CATTANEO A., 2007. Etude préliminaire de l"aléa tsunamis en Méditerranée occidentale - Zonage des mouvements de terrain sous-marins sur le plateau et talus continental au large des côtes françaises". *Rapport final IFREMER, 66p, 2 ann*.

COBURN A. AND SPENCE R. (2002). *Earthquake protection*. 2ème edition, Ed. Wiley.

FEDERAL EMERGENCY MANAGEMENT AGENCY (FEMA), 2004. Using HAZUS-MH for risk assessment (FEMA 433). Report of the Federal Emergency Management Agency, Washington, DC, United States, 224 pp.

GARCIN M., PRAME B., ATTANAYAKE N., DE SILVA U., DESPRATS J.F., FERNANDO S., FONTAINE M., IDIER D., LENOTRE N., PEDREROS R. AND SIRIWARDANA C. (2007). Geographic Information Systems for Coastal Hazards – Application to a pilot zone in Sri Lanka. *Rapport* BRGM 55553.

GIOVINAZZI S., (2005). "The vulnerability assessment and the damage scenario in seismic risk analysis", PhD *Thesis*, Department of Civil Engineering of the Technical University Carolo-Wilhelmina at Braunschweig and the Faculty of Engineering Department of Civil Engineering of the University of Florence.

GUILLANDE R., VALENCIA N. AND GARDI A. (2009). Uncertainties in modelling and damage assessment of tsunami risk, implications for crisis management (FP6 SCHEAMA project). *Poster* à Seismic Risk in Moderate Seismicity areas, Aix en Provence, Juillet 2009.

GUHA-SAPIR D.., PARRY L, DEGOMME O, JOSHI P.C. & SAULINA ARNOLD J.P. (2006). Risk factors for mortality and injury: post-tsunami epidemiological findings from Tamil Nadu. Centre for Research on the Epidemiology Disasters (CRED). http://www.cred.be/sites/default/files/RiskFactorsMortalityInjury.pdf

LAGOMARSINO S., GIOVINAZZI S., (2006). "Macroseismic and mechanical models for the vulnerability and damage assessment of current buildings", *Bull. of Earthquake Engineering*, 4, pp. 445-463.

LAMBERT J., TERRIER M., 2011. Historical tsunami database for France and its overseas territories. *Nat. Hazards Earth Syst. Sci.*, 11, 1037–1046, 2011

IGN (2009). *BD topo version 2, descriptif de contenu.* http://professionnels.ign.fr/DISPLAY/000/506/447/5064472/DC_BDTOPO_2.pdf

KELMAN I. (2002). Physical Flood Vulnerability of Residential Properties in Coastal, Eastern England. *Thesis*, Université de Cambridge.

KOSHIMURA S., KATADA T., MOFIELD H.O. AND KAWATA Y. (2006). - A method for estimating casualties due to the tsunami inundation flow. *Nat Hazards* (2006) 39:265–274.

LEONE F., DENAIN J.C., VINET F. AND BACHRI S., (2006). Analyse spatiale des dommages au bâti de Banda Aceh (Sumatra, Indonésie) : contribution à la connaissance du phénomène et à l' élaboration de scénarios de risque tsunami. *Scientific report of Tsunarisque (2005-2006) program*.

LE ROY S., PEDREROS R., MONFORT-CLIMENT D. (2011). – ALDES : Modélisation numérique du tsunami survenu à Antibes en 1979. Open-file BRGM report BRGM/RP-60353-FR, 80 p., 61 ill. (in french)

MARCHE, F., P. BONNETON, P. FABRIE AND N. SEGUIN (2007). - Evaluation of well-balanced bore-capturing schemes for 2D wetting and drying processes. *International Journal for Numerical Methods in Fluids, 53: 867-894*.

MIMURA N., YASUHARA K., KAWAGOE S.,YOKOKI H. AND KAZAMA S. (2011). Damage from the Great East Japan Earthquake and Tsunami - A quick report. *Mitig Adapt Strateg Glob Change* (2011) 16:803–818.

MONFORT D., TERRIER M., SEDAN O., MARÇOT N. (2010). – Projet RATCOM : Méthode d"évaluation de la vulnérabilité aux tsunamis en Méditerranée occidentale. Rapport BRGM/RP-58595-FR,143p

NISHIKIORI N., ABE T., COSTA D.G., DHARMARATNE S.D., KUNII O. AND MOJI K. (2006). Who died as a result of the tsunami? – Risk factors of mortality among internally displaced persons in Sri Lanka: a retrospective cohort analysis. *BMC Public Health2006*, 6:73 doi:10.1186/1471-2458-6-73

PAPADOPOULUS, G., A. AND FOKAEFS, A. 2005. Strong tsunamis in the Mediterranean Sea: A re-evaluation, ISET Journal of Earthquake Technology: 463/42/2, 159-170

PEDREROS, R ET POISSON, B., 2007. Tsunamis : étude de cas au niveau de la côte méditerranéenne française - Modélisation numérique. Open-file BRGM*,Rapport* BRGM/RP-55760-FR.

PEIRIS N. (2006). Vulnerability functions for tsunami loss estimation. First European conference on Earthquake Engineering and Seismology, a joint event of the 13th ECEE & 30th General Assembly of the ESC), Geneva, Switzerland, Paper number 1121.

ROBERT S., SILLERE G. AND LIZIARD S. (2008). - Évaluer et représenter le nombre d' usagers sur une plage urbaine (Les Ponchettes, Nice). http://mappemonde.mgm.fr/num19/articles/art08305.html

SAHAL A., LEMAHIEU A. (2010). The 1979 Nice airport tsunami : mapping of the flood in Antibes. *Nat hazards*.

SILVA JACINTO R. & MEYNIEL P. (2010). – RatCom – Réseaux d"alerte aux Tsunamis et submersions Côtières en Méditerranée. Modélisation des écoulements gravitaires sous-marins en Baie-des-Anges en vue de la génération de tsunamis dans le champ proche. *R. int Ifremer Brest / GM / LES / 201-08*.

TERRIER M., 2007. Réalisation d"un zonage sismique de la Méditerranée occidentale à 1/2 000 000 préalable aux choix de scénarios de tsunamis. Open-file BRGM*, Rapport* BRGM/RP - 55353 –Fr (in french).

TERRIER M., PEDREROS R. ET POISSON B. (2007). Tsunamis : Étude de cas au niveau de la côte méditerranéenne française - Open-file BRGM report n° BRGM-RP-55765-Fr (in french).

WATTS, P., GRILLI, S.T., KIRBY, J.T., FRYER, G.J., TAPPIN, D.R., 2003. Landslide tsunami case studies using a Boussinesq model and a fully nonlinear tsunami generation model. *Natural Hazards and Earth System Sciences* 3, 391-402.

YANG F., BARRAL J., PREVOST T., LALIGRAND P., MASSART N., SCHMITT V. AND OLLINGER E. (2001). Génération de tsunamis. Nice, 16 octobre 1979. *Rapport de projet scientifique collectif*, Ecole Polytechnique, promotion 2001. Tuteur M. Dias, coordinateur M. Huerre.

ISSN 8755-6839

SCIENCE OF **TSUNAMI HAZARDS**

Journal of Tsunami Society International

Volume 32 **Number 2** **2013**

SEDIMENTARY FEATURES OF TSUNAMI BACKWASH DEPOSITS AS ASSESSED BY MICRO-BEAM SYNCHROTRON X-RAY FLUORESCENCE (μ-SXRF) AT THE SIAM PHOTON LABORATORY

Siwatt Pongpiachan[1], Kanjana Thumanu[2], Waraporn Tanthanuch[2], Danai Tipmanee[3,4], Panatda Kanchai[1], Klaus Schwarzer[5] and Somchai Tancharakorn[2*]

[1]NIDA Center for Research & Development of Disaster Prevention & Management, School of Social and Environmental Development, National Institute of Development Administration (NIDA), 118 Moo-3, Sereethai Road, Klong-Chan, Bangkapi, Bangkok 10240 THAILAND
[2]Synchrotron Light Research Institute (Public Organization), Ministry of Science and Technology, THAILAND
[3]International Postgraduate Program in Environmental Management, Graduate School, Chulalongkorn University, Bangkok, THAILAND
[4]Center of Excellence for Environmental and Hazardous Waste Management (EHWM), Chulalongkorn University, Bangkok, THAILAND
[5]Institute of Geosciences Sedimentology, Coastal and Continental Shelf Research, Christian Albrechts University Kiel, Otto Hahn Platz 1, D - 24118 Kiel, GERMANY

ABSTRACT

Over the past few years, several attempts have been performed to find alternative "*chemical proxies*" in order to discriminate "tsunami backwash deposits" from "typical marine sediments". A wide range of statistical tools has been selected in order to investigate the sediments and/or terrestrial soils transportation mechanism during the tsunami inundation period by using several types of chemical tracers. To relate the physical and chemical characteristics of Typical Marine Sediments (TMS),

[*]Corresponding author landline phone: (66) 44-217040 ext 1477; mobile phone: (66) 860319900; fax: (66) 044-217047; e-mail: somchai@slri.or.th

Tsunami Backwash Deposits (TBD), Onshore Tsunami Deposits (OTD) and Coastal Zone Soils (CZS) with their synchrotron radiation based micro-X-ray Fluorescence (μ-SXRF) spectra, the μ-SXRF spectra were built in the appropriate selected spectra range from 3,000 eV to 8,000 eV. Further challenges were considered by using the first-order derivative μ-SXRF spectra coupled with Probability Distribution Function (PDF), Hierarchical Cluster Analysis (HCA) and Principal Component Analysis (PCA) in order to investigate the elemental distribution characteristics in various types of terrestrial soils and marine sediments. Dendrographic classifications and multi-dimensional plots of principal components (i.e. bi-polar and three dimensional plots) could indicate the impacts of terrestrial soils and/or marine sediments transport on onshore and/or offshore during the tsunami inundation period. Obviously, these advanced statistical analyses are quite useful and provide valuable information and thus shed new light on the study of paleotsunami.

Keywords: *Andaman Sea; Tsunami Backwash Deposits; Micro-beam Synchrotron X-ray Fluorescence (μ-SXRF); First Order Derivative; Hierarchical Cluster Analysis; Principal Component Analysis.*

1. INTRODUCTION

The 2004 Sumatra-Andaman earthquake and tsunami was commonly considered as the worst natural disaster to ever attack Southeast Asian countries, triggering death and injury as well as major destruction to the transportation system, property, and environmental and economic sustainability (Griffin *et al*., 2013; Matsumaru *et al*., 2012). The severe impact on the beach zone between the Pakarang Cape and the Khao Lak, Phang-nga province of Thailand in turn had serious consequences on the scoured features existed in both on the beach side and in the embayment of tidal channels (Choowong *et al*., 2007, 2009; Fagherazzi and Du, 2007). In spite of various papers focusing on geomorphological, sedimentological and geological alterations in tsunami-affected areas (Choowong *et al*., 2007, 2008a, 2008b, 2009;Szczuciński *et al*., 2005, 2006, 2007), the knowledge of chemical distribution is strictly limited.

As a consequence, several challenges have been made to conduct both qualitative and quantitative analyses of various chemical species in both onshore and offshore of tsunami-affected regions (Goff *et al*., 2012; Jagodziński *et al*., 2012; Pongpiachan *et al*., 2012; Pongpiachan *et al*., 2013; Sakuna *et al*., 2012; Tipmanee *et al*., 2012). In order to understand the destructive behaviour of tsunami affecting both onshore and offshore areas, numerous studies have attempted to draw the scientific community's attention on the feasibility of chemical tracers to characterize tsunami backwash deposits from those of typical marine sediments (Pongpiachan *et al*., 2012; Pongpiachan et al., 2013; Tipmanee *et al*., 2012). Since the identification of tsunami backwash deposit is the first step to gain information on tsunami impacts, it is therefore essentially crucial to find an alternative method to discriminate tsunami backwash deposits from those of natural background submarine sediments.

In the past few years, X-ray fluorescence (XRF) have been widely used for the determination of

elements in sedimentological record of tsunamis on the Portuguese Shelf off Lisbon (Abrantes *et al*., 2008), geoarchaeological evidence of multiple tsunamigenic imprint on the Bay of Palairos-Pogonia, Greece (Vött *et al*., 2011)) and most recently sedimentary deposits left by the 2004 Indian Ocean tsunami on the inner continental shelf offshore of Khao Lak, Andaman Sea, Thailand (Sakuna *et al*., 2011). XRF has gained more popularity on studies of environmental sciences because of its relatively low cost solution compared to other analytical instruments, non-destructive testing solution, fast processing time, typical detection limit of around 0.01% for most elements and quantitative analysis. Recently, the shared use of synchrotron radiation based micro-X-ray Fluorescence (μ-SXRF) permits analysis of objects at the micron-scale owing to its high intensity and energy tenability in comparison with those of conventional light sources such as sealed-tube or rotating-anode generators (Tancharakorn *et al*., 2012). Because of micrometer sized X-ray beam, one can use μ-SXRF not only to quantify the elemental compositions in target samples but also its distribution at the micrometer scale (Kanngießer & Haschke, 2006).

In this research, the author postulates that the use of μ-SXRF in cooperation with the first derivative, probability distribution functions (PDF), hierarchical cluster analysis (HCA) and principal component analysis (PCA) provides a better insight of sedimentary features of tsunami backwash deposits in comparison with those of typical marine sediments and terrestrial components. Note that this is the first time to employ μ-SXRF with assistance of synchrotron radiation in order to assess the elemental distribution of tsunami backwash deposits in micro-scale. It is also worth mentioning that neither the source apportionment, nor the analysis of spatial variation of chemical components in sediments is the principal objective of this paper.

2. MATERIALS & METHODS

2.1 Sampling sites & sampling procedure

2.1.1 Surface marine sediment

The research area is governed by two seasonal monsoons: the northeast monsoon from mid October until March and the southwest monsoon from May to September. This study was carried out offshore along the west coast of Phang Nga province, in the southwest region of Thailand, which was heavily affected by the 2004 tsunami. The research area covers approximately 1,000 km^2 between Thap Lamu and Pakarang Cape, up to a water depth of 70 meters. Our research was carried out on research cruises taken from one year apart, from November-December 2007 with RV CHAKRATONG TONGYAI and November-December 2008 with RV BOONLERT PASOOK, covering approximately 1500 nautical miles of hydroacoustic profiles (side scan sonar, multibeam echo sounder and shallow reflection seismic with a boomer system) were recorded at Pakarang Cape. Twenty of sediment samples were collected during 18-20 July 2009 (Fig. 1)). The sampling stations were selected on the basis of the basic data acquired from hydroacoustic mapping using equipment, which consisted of Multi-beam, Side Scan Sonar and Boomer system to investigate the sedimentary deposition on near-

shore seabed (Feldens *et al*., 2009; Feldens *et al*., 2012). These supporting data provided the geophysical structure of seabed, which was promising evidence of terrestrial deposits in the study area. Van-veen Grab Sampler was used to collect the 20 surface sediment samples. Sediment samples were wrapped in clean aluminum foil, placed in a glass bottle, and kept frozen at – 20 ºC.

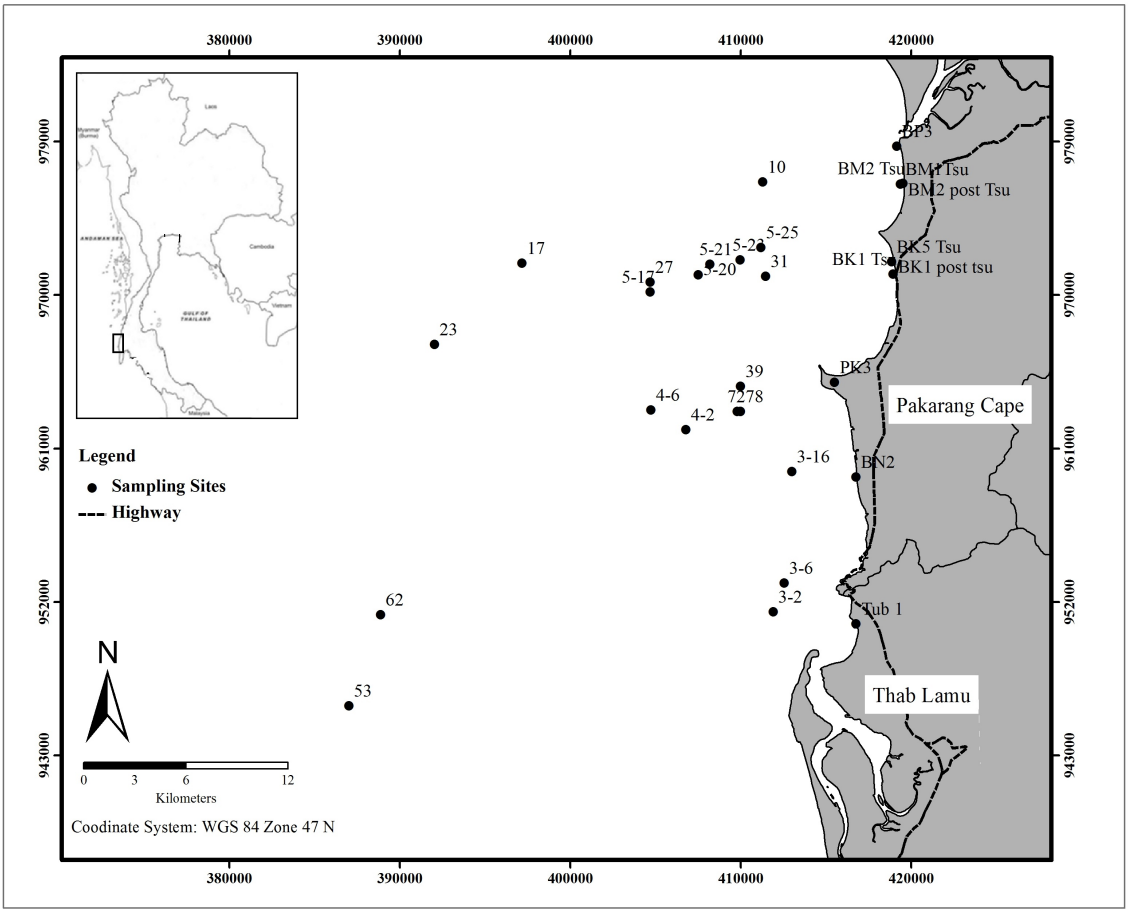

Fig. 1: Sampling site description at tsunami affected area at Khao Lak, Phang-nga province of Thailand.

2.1.2 Terrestrial soils

Ten of terrestrial soil samples were collected during 18-20 July 2009. Soil sampling stations were selected by considering the areas, which were affected by the 2004 Tsunami (Szczucinski *et al*., 2005). In addition, the locations of soil sampling stations were also in the transect line of the surface sediment sampling stations (Fig.1-2). They were collected during 18-20 July 2009. The surface layer was collected by using a clean shovel. About half kilogram of composite samples from 2 m^2 area of each station was taken (Badin *et al*., 2008). They were wrapped in clean aluminum foil, placed in a glass bottle, and kept frozen at - 20ºC

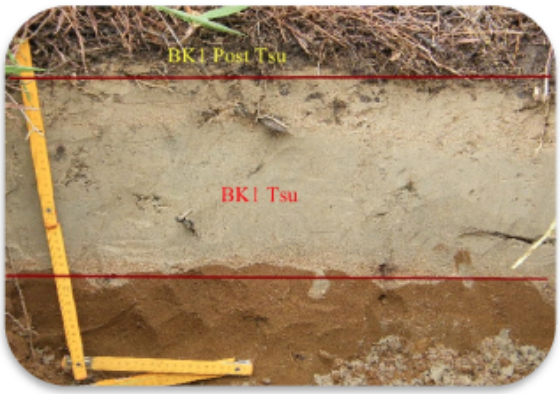

Tsunami deposition layer at station BK 1. (BK1 Post Tsu and BK1Tsu layer)

Tsunami deposition layer at station BK 5. (BK5 Tsu layer)

Tsunami deposition layer at station BM 1. (BM1 Tsu layer)

Tsunami deposition layer at station BM 2 (BM2 Post Tsu and BM2Tsu layer)

Fig. 2: Tsunami and Post-tsunami deposition layer at Khao Lak, Phang-nga province of Thailand.

2.2 Sample preparation for μ-SXRF

Due to the heterogeneity of sediment, all samples for XRF measurement were prepared in homogenous and flat discs using grinding and pelletizing processes. In the grinding process, 100 g of powder was weighted and put into a 10 ml ZrO_2 grinding bowl with two ZrO_2 balls (Ø 10 mm) and seven SiO_2 balls (Ø 5 mm) and shaken at 1,800 oscillations/min for 30 minutes (Fig. 3). Then, in the pelletizing process, 50 g of homogenous powder was put into a steel mould and pressurized at 4 tons for 1 minute to form a 13 mm in diameter disc.

Fig. 3: sediment powder with grinding balls in a ZrO2 bowl before (a) and after (b) grinding process, and after (c) pelletizing process.

2.3 μ-SXRF Experiment

Synchrotron X-ray fluorescence experiments were carried out at the μ-SXRF end-station (Tancharakorn *et al*., 2012) attached to beamline 2.2 of the Siam Photon Laboratory to utilize monochromatic X-ray beam. In this beamline, X-rays can be generated by the 1.2 GeV storage ring travelling 21 m through an evacuated pipe to the sample. The beamline consists of a double multilayer monochromator (DMM) (at 8.8 m downstream) to select desired energy between 6 keV to 9 keV, focusing mirror (FM) (at 11.0 m downstream) to increase photon flux and beryllium window of 200 μm thickness (at 21 m downstream) to separate high vacuum region and atmospheric pressure. Details of the beam line 2.2 can be found in previous literature (Soontaranon *et al*., 2012). In the experiment, samples were mounted on a motorized sample stage in air. An energy-dispersive Si-PIN detector from AMPTEK, USA, with energy resolution of 160 eV at the Mn K_{α} emission line was used to collect XRF signals. Six spots were randomly chosen to be exposed with 9 keV X-rays for 100 seconds for each spot. XRF signals were collected in the detector and then sent to MCA8000A multichannel analyzer (AMPTEK, USA) where each signal is stored in each channel corresponding to the certain energy. Therefore, the detector must be first calibrated to find a relationship between channel and photon energy. Here commercial XRF metal standards (titanium, vanadium and iron foils) were used. The energy-dispersive data were finally created in a single-column file, which can be analyzed using the *pyMCA*. In this code, a Guassian function is used to characterized position, width and height or area of each peak. The position of each peak is used to identify element, while its area is directly related to its concentration. The code also deals with the background signal. The algorithm of the pyMCA can be found in (Sole *et.al*., 2007).

2.4 Statistical analysis

The derivative spectrophotometric method is based on transformation of zero-order spectra of sediment and soil samples into the first-order derivative (ΔPhoton Energy (eV)/ΔIntensity (counts)). In this study, the value of first derivative was performed by using the Software OPUS Version 7.0. In addition, first derivatives of the spectral data from each sampling location were treated through hierarchical cluster analysis (HCA) and principal component analysis (PCA) with the orthogonal Varimax solution using Statistical Package for the Social Sciences (SPSS) Version 13.0.

3. RESULTS & DISCUSSION

3.1.Characteristics of the first-order derivative μ-SXRF spectra

Although several attempts have been made by several researchers to quantify chemical contents in sediments in order to elucidate tsunami backwash mechanism (Pongpiachan *et al*., 2012; Pongpiachan *et al*., 2013; Sakuna *et al*., 2012; Tipmanee *et al*., 2012;), some alternative proxies are always required to enhance the reliability of data interpretation. In this study, the assessment of μ-SXRF spectra as an alternative "fingerprint" to discriminate tsunami backwash deposit from typical marine sediments was performed by using the concept of first derivative. All samples were classified into four groups namely "Typical Marine Sediments (TMS)", "Tsunami Backwash Deposits (TBD)", "Onshore Tsunami Deposits (OTD)" and "Coastal Zone Terrestrial Soils (CTS)" as clearly described in Table 1.

Table 1. Sample information of marine sediments and terrestrial soils.

Sampling code	Sampling date	Sampling description
Coastal Zone Soils (CZS)		
Tub1	July-18-2009	Canal bank
PK 3	July-19-2009	Shrimp pond
BN 2	July-20-2009	Canal bank
BP 3	July-20-2009	Mangrove
Onshore Tsunami Deposits (OTD)		
BK 1 Post Tsu, BK1 Tsu	July-19-2009	Tsunami deposit layer
BK 5 Tsu	July-19-2009	Tsunami deposit layer
BM 1 Tsu	July-20-2009	Tsunami deposit layer
BM 2 Post Tsu, BM2 Tsu	July-20-2009	Pond

Typical Marine Sediments (TMS)		
10, 17	December-1-2007	Pakarang cape sediment
3-2 ,3-6, 3-16, 4-2, 4-6, 5-20, 5-25	March-4-5- 2010	Pakarang cape sediment
53, 62	December-7-2007	Thup Lamu Sediment
Tsunami Backwash Deposits (TBD)		
23, 27, 31, 39, 72, 78	December-3-2007	Tsunami affected sediment
5-17, 5-21, 5-23	March-5- 2010	Tsunami affected sediment

The average μ-SXRF spectra of four sample groups are compared and carefully investigated (See Fig. 4). Generally, all sample groups display similar spectral characteristics. There are four prominent features, which are common to all μ-SXRF spectra: *a*) main element which can be found in all samples is calcium (K_α at 3.69 keV, K_β at 4.01 keV); *b*) all samples have a relatively small amount of titanium (K_α at 4.51 keV, K_β at 4.93 keV) and manganese (K_α at 5.90 keV, K_β at 6.49 keV); *c*) another main element contained in all samples is iron(K_α at 6.40 keV, K_β at 7.06 keV); and *d*) low concentration of three elements which are potassium ((K_α at 3.31 keV, K_β at 3.59 keV), titanium and manganese were detected in OTD samples. Based on these results, one can deduce that all elemental species in samples share comparable distribution patterns.

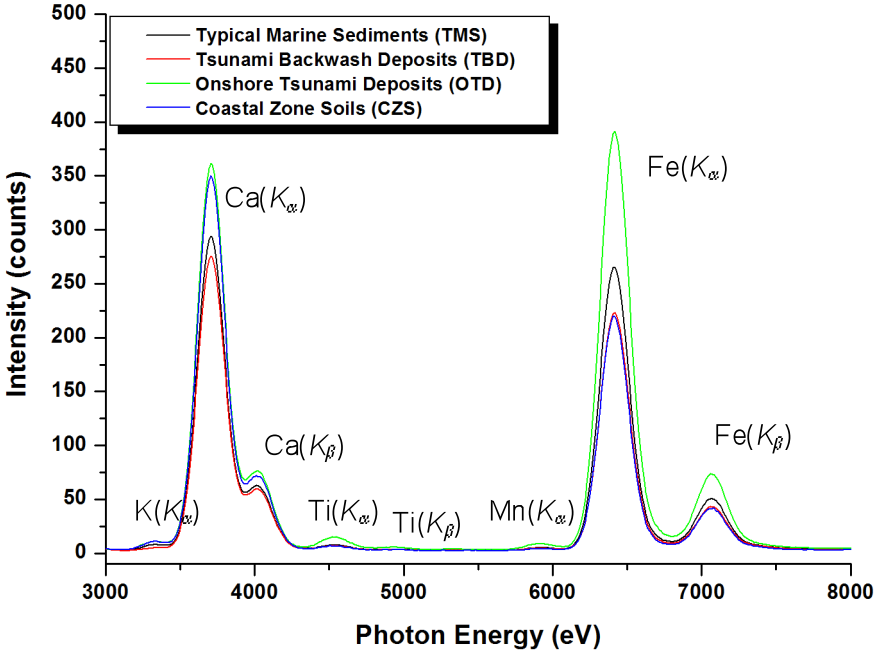

Fig. 4: μ-SXRF spectra of typical marine sediments (TMS), tsunami backwash deposits (TBD), on-shore tsunami deposits (OTD) and coastal zone soils (CZS).

Although all sample groups show comparatively similar μ-SXRF spectra features in the photon energy range from 3000 to 8000 eV, some subtle relative changes can be enhanced by computing the first-order derivative of raw spectra (Balsam and Deaton, 1991). The computation of the first-order derivative generates curves that have peaks where the rate of change of the raw μ-SXRF spectral curves is at maximum and are flat where spectral curves display no change in slope. TMS is characterized by its four positive major peaks in the first derivative situated at 5104 eV, 5165 eV, 5735 eV and 7754 eV, followed by three negative main peaks located at 3110 eV, 5091 eV and 5661 eV respectively. On the contrary, the disappearances of two main peaks at 3110 eV and 7754 eV were detected at TBD, OTD and CZS samples, highlighting the absence of some typical marine elements in non-marine samples. It is well known that marl and calcareous clay, glauconite, kalolinite, organic matter, phosphorite, hematite and goethite show relatively high contribution in marine sediments as previously mentioned in several publications (Balsam and Beeson, 2003). Recent studies also reveal the significance of Ca, Fe, K, Sr, and Ti in selected sediment sections from a continental margin sediment core by using Micro-XRF analyzer (Micro-XRF) with a 100-μm resolution and an XRF whole-core scanner (XRF-S) with a 5-mm resolution (Böning *et al*., 2007). Hence, the discrepancy of μ-SXRF spectra features between marine and non-marine samples can be ascribed to the differences in elemental compositions.

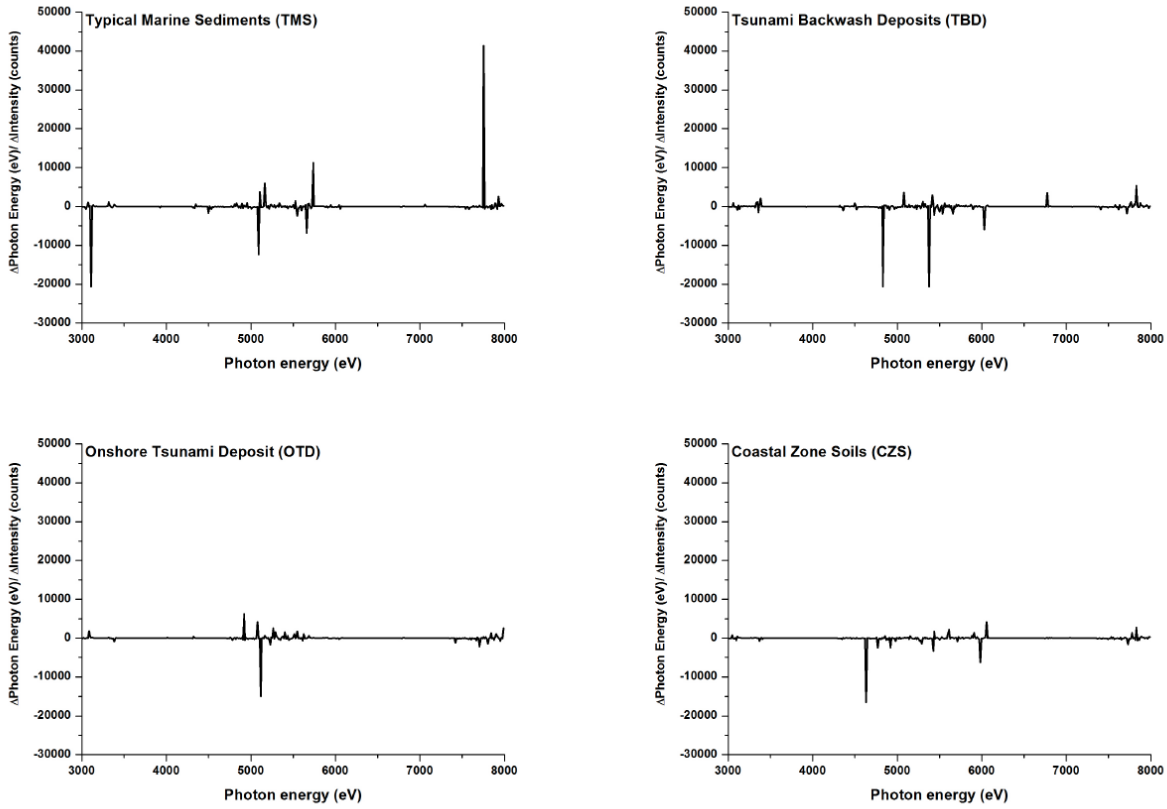

Fig. 5: First derivative plot of typical marine sediments (TMS), tsunami backwash deposits (TBD), on-shore tsunami deposits (OTD) and coastal zone soils (CZS).

3.2 Probability distribution function (PDF)

In probability theory, a probability density function (PDF) is a function that defines the comparative possibility for this random variable to take on a certain value. The probability for the random variable to fall within a particular region is given by the integral of this variable's density over the region. The probability density function is nonnegative everywhere, and its integral over the entire space is equal to one. PDF was employed to all μ-SXRF spectra in the intensity range from 0 to 400 counts as clearly displayed in Fig. 6. Generally, the probability density of standard normal distribution can be described as follows:

$$f(x) = \frac{1}{\sqrt{2\pi}} e^{\frac{-x^2}{2}} \tag{1}$$

where e, x and π represent for exponential constant (i.e. 2.718), intensity (counts) and pi value (i.e. 3.142) respectively. If a random variable X is provided and its distribution possesses a probability density function f, then the estimated value of X can be computed as

$$E[X] = \int_{-\infty}^{\infty} x f(x) dx \tag{2}$$

A distribution has a density function if and only if its cumulative distribution function $F(x)$ is absolutely continuous. In this case: F is almost everywhere differentiable, and its derivative can be used as probability density:

$$\frac{d}{dx} F(x) = f(x) \tag{3}$$

PDF is a function that describes the relative likelihood for this random variable to take on a given value. The probability for the random variable to fall within a particular region is given by the Gaussian distribution, which can be described as follows:

$$y = \frac{1}{\sigma\sqrt{2\pi}} \exp\left(\frac{-(x-\mu)^2}{2\sigma^2} \right) \tag{4}$$

where y, σ, σ^2, μ and x represent for probability distribution function (PDF), standard deviation of μ-SXRF spectra intensity, variance of μ-SXRF spectra intensity, average of μ-SXRF spectra intensity and μ-SXRF spectra intensity of all samples respectively.

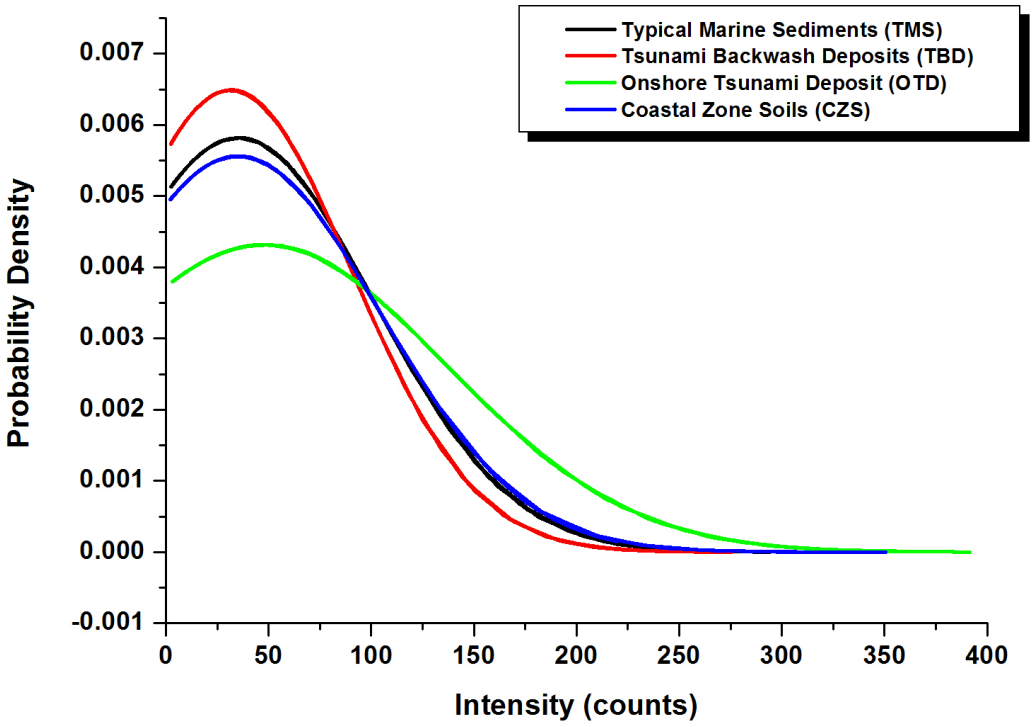

Fig. 6: Probability distribution of μ-SXRF of typical marine sediments (TMS), tsunami backwash deposits (TBD), on-shore tsunami deposits (OTD) and coastal zone soils (CZS).

As noticeably displayed in Fig. 6, some prominent curve features can be obtained directly from these unique plots. It is worth mentioning that "*skewness*" is a degree of the asymmetry of the curve plots between μ-SXRF spectra intensity and PDF of a real-valued random variable (i.e. μ-SXRF spectra intensity). Basically, there are three types of "*skewness*" values, which can be termed as positive skew, negative skew and undefined. A positive skew designates that the tail on the right side is longer than the left side, whilst a negative skew implies that the tail on the left side is longer than the right side. It is also important to stress that the bulk of the PDF values (including the median) of positive skew and negative skew situate at the left and right of the mean respectively. Qualitatively, a zero value implies that the PDF values are comparatively consistently dispersed on both sides of the mean, characteristically indicating a symmetric distribution.

Firstly, the relatively symmetrical bell-shape curves were detected in the curve plots between averaged μ-SXRF spectra intensity and PDF of TMS, TBD and CZS with moderately longer tails in the right side with most of the data still concentrated on the left indicating the "*positive skewness*" type of normal distribution. Since the majority of the PDF curve peaks are more focused in the intensity range of 50 ± 5 counts, it seems rational to assume that this phenomenon is a consequence of comparatively homogeneous spatial elemental distribution in typical marine sediments, tsunami

backwash deposits and coastal zone soils. Interestingly, both TMS and CZS have considerably similar curve plots in spite of its different sampling backgrounds. This can be explained by the invariability of elemental compositions (i.e. Cl, K, Ca, Ti, Cr, Mn, Fe, V) observed in both marine sediments and terrestrial soils. Secondly, the irrelevant curve feature of OTD was detected with "*positive skewness*" type of bell shape distribution with exceedingly broad peaks coupled with flat tops at the interval range of 50 to 300 counts in comparison with those of TMS, TBD and CZS. This reflects highly deviated elemental distributions involved in onshore tsunami deposits as a result of more complex chemical mixtures derived from both terrestrial components and marine deposits.

3.3 Hierarchical cluster analysis (HCA)

Cluster analysis (CA), also called segmentation analysis or taxonomy analysis, seeks to identify homogeneous subgroups of cases in a population. That is, cluster analysis seeks to identify a set of groups, which both minimize within-group variation and maximize between-group variation. In this study, CA was conducted using SPSS 13.0 for Windows. CA techniques may be *hierarchical* (i.e. the resultant classification has an increasing number of nested classes) or *non-hierarchical* (i.e. *k*-means clustering). *Hierarchical clustering* allows users to select a definition of distance, then select a linking method of forming clusters, then determine how many clusters best suit the data. *Hierarchical clustering* methods do not require pre-set knowledge of the number of groups.

Two general methods of *hierarchical clustering* methods are available: divisive and agglomerative. The divisive technique starts by assuming a single group, partitioning that group into subgroups, partitioning these subgroups further into subgroups and so on until each object forms its own subgroup. The agglomerative techniques start with each object describing a subgroup, and then combine like subgroups into more inclusive subgroups until only one group remains. In either case, the results of the application of the clustering technique are best described using a dendrogram or binary tree. The objects are represented as nodes in the dendrogram and the branches illustrate when the cluster method joins subgroups containing that object. The length of the branch indicates the distance between the subgroups when they are joined.

In this study, Hierarchical Cluster Analysis (HCA) was applied to test the hypothesis that μ-SXRF spectra can be used as an alternative "*fingerprint*" in order to distinguish "tsunami backwash deposits" from those of "typical marine sediments". Two types of datasets, namely raw and first derivative μ-SXRF spectra of all samples, were employed to HCA as clearly illustrated in Fig. 7-8. The HCA of raw μ-SXRF spectra showed the existence of two major clusters with four different sub-clusters. The first main cluster constitutes[consists of?] of all sample types with the average percentage contribution of 37 %, 21 %, 26 % and 16% for TMS, TBD, OTD and CZS respectively. This cluster can be divided into two sub-clusters; the first sub-cluster constitutes of TMS (30 %), TBD (20 %), OTD (40 %), CZS (10 %) and the second sub-cluster is composed of TMS (44 %), TBD (22 %), OTD (11 %), CZS (22 %). According to dendrogram, the second major cluster [is constructed of?]constructs of all groups with the average percentage contribution of 35 %, 48 %, 8 % and 8% for TMS, TBD, OTD and CZS respectively. The second major cluster can be separated into two sub-

clusters; the third sub-cluster [is comprised of?]comprises of TMS (20 %), TBD (80 %), OTD (0 %), CZS (0 %) and the fourth sub-cluster is composed of TMS (35 %), TBD (48 %), OTD (8 %), CZS (8 %). The second major cluster can be considered as a mixture of "typical marine sediments" and "tsunami backwash deposits", which has been highly characterized in the third sub-cluster (See Fig. 7).

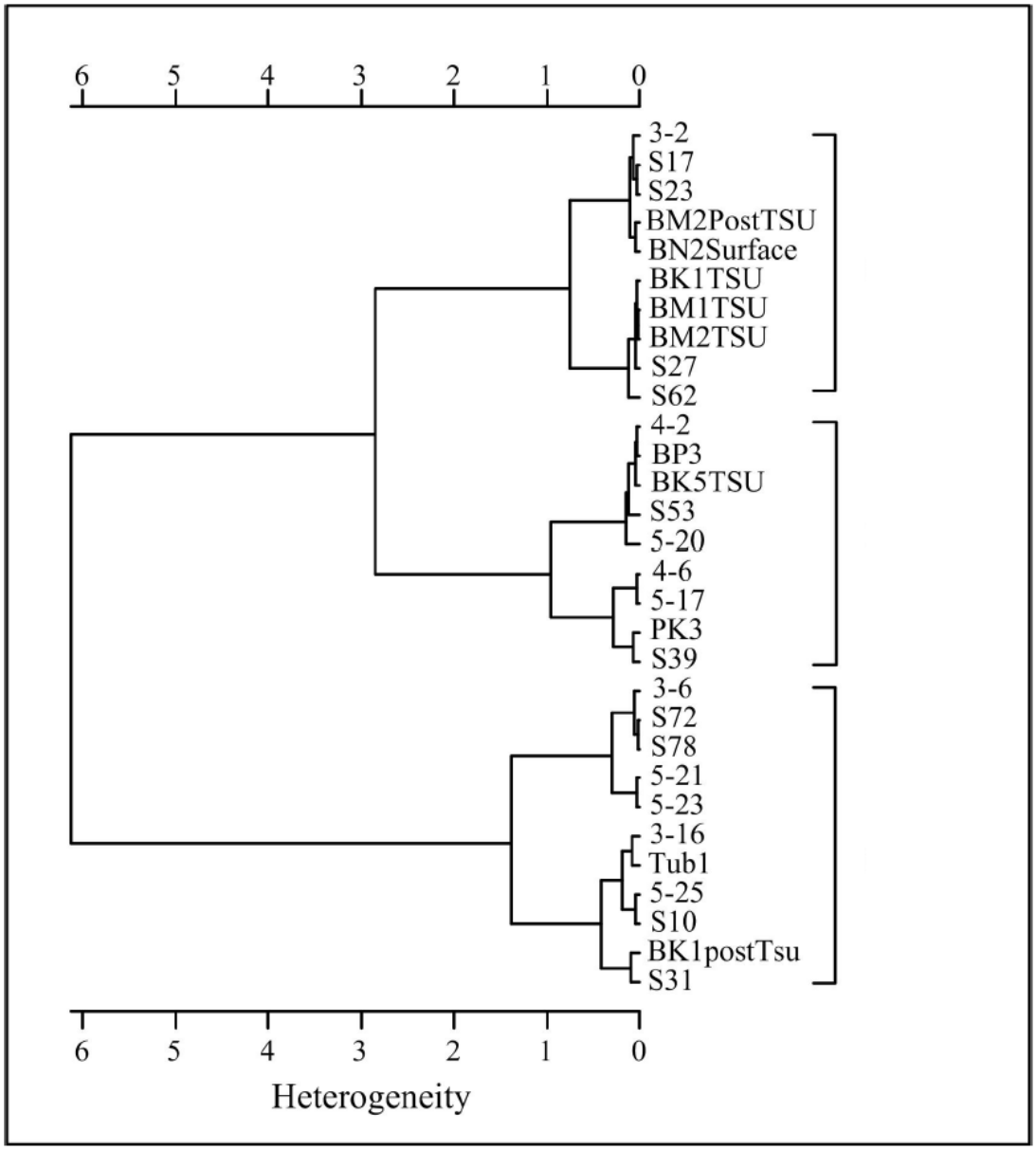

Fig. 7: Dendrographic classification with raw data of typical marine sediments (TMS), tsunami backwash deposits (TBD), on-shore tsunami deposits (OTD) and coastal zone soils (CZS). The Euclidean distance after vector normalization spectra and the Ward linkage method were employed. For details about cluster group composition see data in Table 1.

Further efforts to underline the importance of μ-SXRF spectra as an alternative "*fingerprint*" have been conducted by using the first derivative data. It can be seen in Fig. 8 that the OTD samples are highly deviated from CZS samples, which emphasizes the strong discrepancy in elemental distribution between onshore tsunami deposits and coastal zone soils. Interestingly, TMS samples have a high degree of similarity with those of OTD samples. This particular phenomenon can be ascribed as heavily influenced by advancement of large-scale tsunami inundation, which is responsible for extensive sediment transport from the offshore and subsequently deposited over the coastal areas. Similarly, TBD samples share a high level of affinity with those of CZS samples. This unique occurrence can be attributed to rapid tsunami backwash, which carried terrestrial debris from the onshore to the offshore.

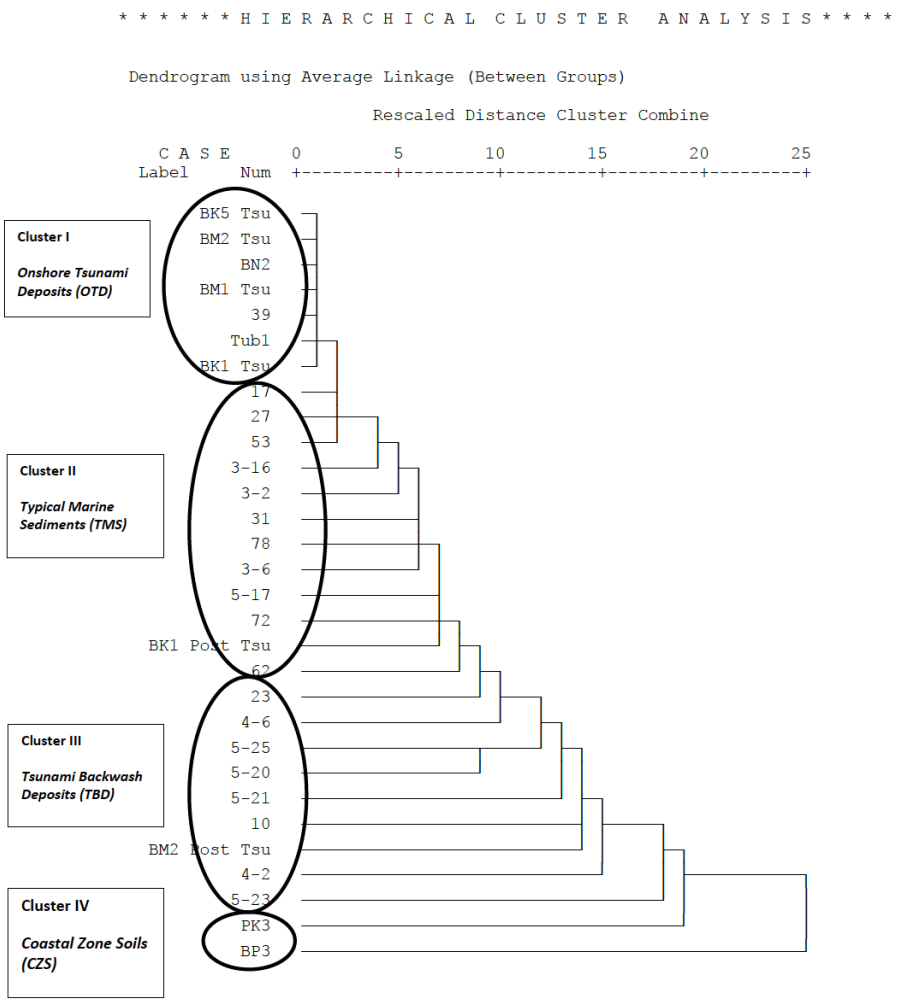

Fig. 8: Dendrographic classification with the first-order derivative data of typical marine sediments (TMS), tsunami backwash deposits (TBD), on-shore tsunami deposits (OTD) and coastal zone soils (CZS). The Euclidean distance after vector normalization spectra and the Ward linkage method were employed. For details about cluster group composition see data in Table 1.

3.4 Principal component analysis (PCA)

In PCA, all variables are expressed in standardized form with a mean of 0 and a standard deviation of 1. The total variance therefore equals the total number of variables, and the variance of each factor expressed as a fraction of the total variance is referred to as the eigenvalue. If a factor has a low eigenvalue, then it is contributing little to the explanation of variances in the variables and may be ignored. PCA is generally used when the research purpose is data reduction (i.e. to reduce the information in many measured variables into a smaller set of components). PCA seeks a linear combination of variables such that the maximum variance is extracted from the variables. It then removes this variance and seeks a second linear combination that explains the maximum proportion of the remaining variance, and so on. This is called the principal axis method and results in orthogonal (uncorrelated) factors. Thus, the largest combination, accounting for most of the variance, becomes principal component 1 (PC1), the second largest accounts for the next largest amount of variances and becomes principal component 2 (PC2), and so on. In general, the first component (P_1) for observed variables X_1, X_2, ……, X_p can be expressed as:

$$P_1 = a_{(1)1}X_1 + a_{(1)2}X_2 + ... + a_{(1)p}X_p \tag{5}$$

where the $a_{(1)1}, a_{(1)2}, ..., a_{(1)p}$ are the weights chosen to maximise the ratio of the variance of P_1 to the total variation, subject to the constraint that

$$\sum_{i=1}^{p} a_{(1)i}^2 = a_{(1)}^t a_{(1)} = 1 \tag{6}$$

The second principal component (P_2) is the combination of the observed variables, which is uncorrelated with the first linear combination and which accounts for the maximum amount of the remaining total variance not already accounted for by P_1. Assume that the data set has n samples for p variables. The basic ($n \times p$) data matrix can be written as:

$$\underset{(n\times p)}{X} = \begin{bmatrix} X_{11} & X_{12} & ... & ... & X_{1p} \\ X_{21} & X_{22} & ... & ... & X_{2p} \\ ... & ... & ... & ... & ... \\ ... & ... & ... & ... & ... \\ X_{n1} & X_{n2} & ... & ... & X_{np} \end{bmatrix} \tag{7}$$

where X_{ij} is the value of variable j obtained for sample i. When the matrix X is used, P can be rewritten as:

$$P = (X - M)A \tag{8}$$

where M is the mean matrix given by:

$$\underset{(n\times p)}{M} = \begin{bmatrix} \overline{X_1} & \overline{X_2} & \ldots & \ldots & \overline{X_p} \\ \overline{X_1} & \overline{X_2} & \ldots & \ldots & \overline{X_p} \\ \ldots & \ldots & \ldots & \ldots & \ldots \\ \ldots & \ldots & \ldots & \ldots & \ldots \\ \overline{X_1} & \overline{X_2} & \ldots & \ldots & \overline{X_p} \end{bmatrix} \tag{9}$$

where Equation 9 is the mean for variable j.

$$\overline{X_j} = \left(\frac{1}{n}\right)\sum_{i=1}^{n} X_{ij} \tag{10}$$

The matrix of *standardised loadings*, A, is a ($^{p\times p}$) matrix such that $A^T A = I$. The *scores matrix*, P, is a ($^{n\times p}$) matrix such that $P^T P$ is a diagonal matrix. Equation 7 becomes

$$X = M + PA^T \tag{11}$$

In this study, Varimax rotation was selected to maximize the sum of the variances of the squared loadings and thus enable us to seek the similarity of chemical components in sediment and soil samples. μ-SXRF spectra of the samples listed in Table 1 were analysed by PCA. The principal component patterns for Varimax rotated components of 30 samples composed of two PC, which account for 82.9 % and 17.0 % for the total of variances of PC1 and PC2 respectively. The contribution of PC1 and PC2 explains 99.9 % of total variance, and moreover PC1 is 4.87 times higher than PC2.

Multi dimensional (MD) plots of PC1, PC2 and PC3 have been frequently employed as diagnostic tools of chemical sources in environmental samples (Marcosa *et al*., 2010; Pongpiachan, 2006; Pongpiachan *et al*., 2012; Pongpiachan *et al*., 2013; Tipmanee *et al*., 2012). MD distribution patterns of PCs can be used as a characteristic diagnostic parameter to identify their elemental distribution characteristics in soil and sediment samples. However, these MD plots, as well as HCA and PDF, should be used with great caution as physiochemical processes can alter elemental distribution pattern during their transport from the emission source to the receptor site. Apart from using only raw data of μ-SXRF spectra, a second approach was also pioneered by using the first-order derivative dataset for three-dimensional (3D) plots of PCs in order to minimize the above-mentioned uncertainties.

In bi-polar plots of PC1 versus PC2 (see Figure 9), the vast majority of data points were clustered along the positive values of PC2 (y-axis) adjacent to 1.0 and subsequently decrease exponentially to positive side of PC1 (x-axis). The clearest features in MD plots (see Fig. 9-10) are: (*i*) 2D plots of samples No.23, No.31, No.39, No.72, No.78, No.5-21 and No.5-23, which were clustered close to

each other. It seems rational to interpret this cluster as evidence of tsunami backwash deposit samples. (*ii*) 2D plots of CZS samples (i.e. No.Tub1, No.PK3, No.BN2, No.BP3) with the mixture of TMS samples (i.e. No.17, No.53, No.62) and OTD samples (i.e. No. BM1-Tsu, No.BM2-Tsu, No.BP3, No.BK5-Tsu, No.BM2-Post-Tsu). It appears reasonable to ascribe this cluster as a mixture of terrestrial components and marine deposits. This can be deduced as a consequence of inferior mixing process between tsunami backwash deposits and typical marine sediments after tsunami inundation; (*iii*) OTD samples are highly deviated from TMS and TBD samples but possess similar distribution pattern with those of CZS samples as noticeably illustrated in 3D plots of first-order derivative PCs (see Fig. 10). This can be explained by the high degree of similarity in elemental distribution between onshore tsunami deposits and coastal zone soils.

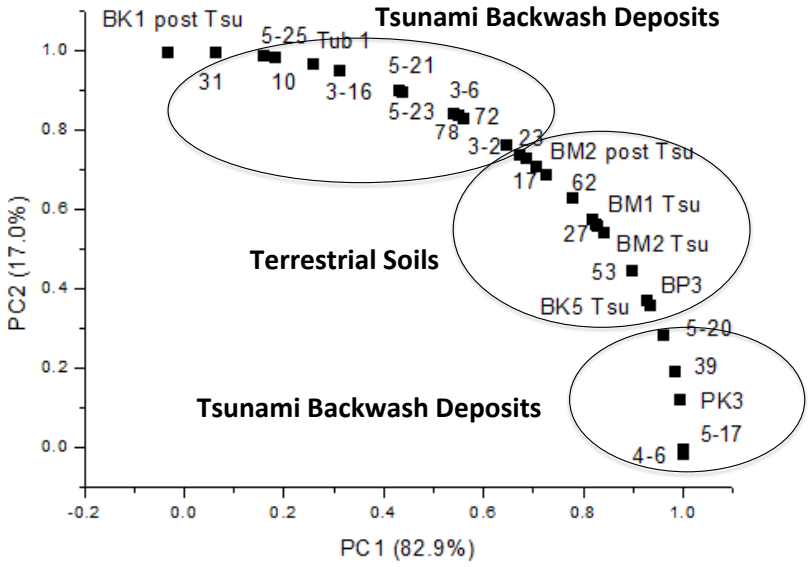

Fig. 9: Three-dimensional plots of principal components (PC) with raw data of typical marine sediments (TMS), tsunami backwash deposits (TBD), on-shore tsunami deposits (OTD) and coastal zone soils (CZS).

4. SYNTHESIS AND CONCLUSIONS

The above statistical analysis of collected data reveals that μ-SXRF spectra can yield authentic and valuable insight upon the terrestrial soils and/or marine sediments transportation processes affecting elemental distribution in the tsunami affected area. Subsequently, the authors support interpreting μ-SXRF spectra on the basis of various types of advanced statistical analyses rather than the simple use of raw spectra, which seems to be difficult for drawing any conclusions.

The major conclusions that occur from this data interpretation are described as follows:

(a) The prominent μ-SXRF spectra features of Typical Marine Sediments (TMS), Tsunami Backwash Deposits (TBD), Onshore Tsunami Deposits (OTD) and Cluster Zone Soils (CZS) can be achieved only through the employment of first order derivative data.

(b) The analysis of Probability Distribution Function (PDF) for different sample categories shows a clear influence of terrestrial soils and/or marine sediments transportation on elemental distribution.

(c) The Hierarchical Cluster Analysis (HCA) analysis of both raw and first order derivative data successfully discriminate terrestrial components from typical marine sediments with the assistance of dendrographic classification.

(d) The multi-dimensional plots of principal components (PCs) by using both raw and first order derivative data highlights the characteristic features of onshore tsunami deposits and coastal zone soils as clearly demonstrated in Fig.9-10.

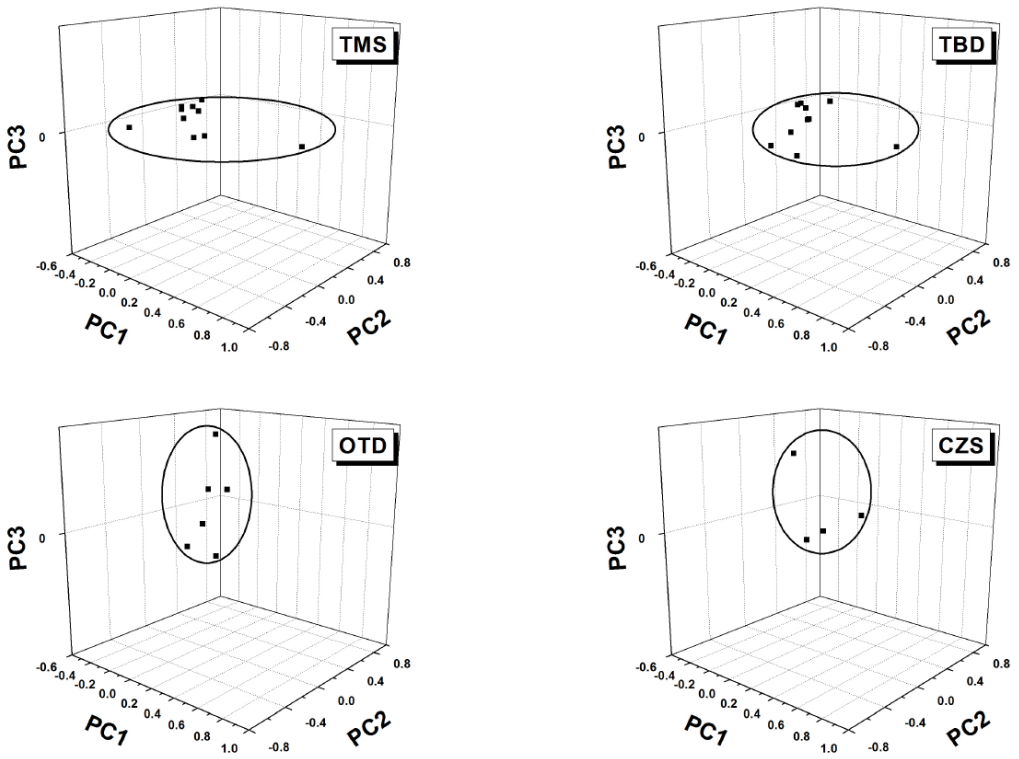

Fig. 10: Three-dimensional plots of principal components (PC) with the first-order derivative data of typical marine sediments (TMS), tsunami backwash deposits (TBD), on-shore tsunami deposits (OTD) and coastal zone soils (CZS).

5. ACKNOWLEDGEMENTS

This work was performed with the approval of Deutsche Forschungsgemeinschaft (DFG, Grant SCHW/ 11-1) and National Research Council of Thailand (NRCT). The authors acknowledge Phuket Marine Biological Center (PMBC) for their support with ship time of RV Chakratong Tongyai and RV Boonlert Pasook, as well as other contributions and facilities during field measurements. We are greatful to Mrs. D. Sakuna for support during all cruises. The authors would also like to express special gratitude to Synchrotron Light Research Institute (Public Organization), Ministry of Science and Technology, Thailand for their contribution of μ-SXRF measurements.

REFERENCES

ABRANTES, F., ALT-EPPING, U., LEBREIRO, S., VOELKER, A. & SCHNEIDER, R. (2008). *Mar. Geol*. **249 (3–4)**, 283-293.

BADIN, A. L., FAURE, P., BEDELL, J. P. & DELOLME, C. (2008). *Sci. Total. Environ*. **403**, 178-187.

BALSAM, W. L. & DEATON, B. C. (1991). *Rev. Aquat. Sci*. **4**, 411-447.

BALSAM, W. L. & BEESON, J. P. (2003). *Deep. Sea. Res. Pat. I*. 50, 1421-1444.

BÖNING, P., BARD, E. & ROSE, J. (2007). *Geochem. Geophy. Geosy*. **8 (5)**, DOI: 10.1029/2006GC001480.

CHOOWONG, M., MURAKOSHI, N., HISADA, K., CHARUSIRI, P., DAORERK, V., CHAROENTITIRAT, T., CHUTAKOSITKANON, V., JANKAEW, K. & KANJANAPAYONT, P. (2007). *J. Coastal. Res*. **23(5)**, 1270–1276.

CHOOWONG, M., MURAKOSHI, N., HISADA, K., CHARUSIRI, P., CHAROENTITIRAT, T., CHUTAKOSITKANON, V., JANKAEW, K., KANJANAPAYONT, P. & PHANTUWONGRAJ, S. (2008a) *Mar. Geol*. **248 (3–4)**, 179–192.

CHOOWONG, M., MURAKOSHI, N., HISADA, K., CHAROENTITIRAT, T., CHARUSIRI, P., PHANTUWONGRAJ, S., WONGKOK, P., CHOOWONG, A., SUBSAYJUN,R., CHUTAKOSITKANON, V., JANKAEW, K. & KANJANAPAYONT, P. (2008b). *Terra. Nova*. **20**, 141–149.

CHOOWONG, M., PHANTUWONGRAJ, S., CHAROENTITIRAT, T., CHUTAKOSITKANON, V., YUMUANG, S. & CHARUSIRI, P. (2009). *Geomorphology*. **104**, 134–142.

FAGHERAZZI, S. & DU, X. (2007). *Geomorphology*. **99**, 120-129.

FELDENS, P., SCHWARZER, K., SZCZUCIŃSKI, W., STATTEGGER, K., SAKUNA, D. & SOMGPONGCHAIYKUL, P. (2009). *Polish. J. Enivron*. **18**, 63-68.

FELDENS, P., SCHWARZER, K., SAKUNA, D., SZCZUCIŃSKI, W. & SOMPONGCHAIYAKUL, P. (2013). *Earth. Planets. Space.* **64(10)**, 875-887.

GOFF, C. C., ANDREW, A., SZCZUCIŃSKI, W., GOFF, J. & NISHIMURA, Y. (2012). *Sediment. Geol.* 282, 65-77.

GRIFFIN, C., ELLIS, D., BEAVIS, S. & NANTES, Z.D. (2013). *Ocean. Coast. Manage*. **71**, 176-186.

JAGODZIŃSKI, R., STERNAL, B., SZCZUCIŃSKI, W., GOFF, C. C. & SUGAWARA, D. (2012). *Sediment. Geol*. **282**, 57-64.

KANNGIEβER, B. & HASCHKE, M. (2006). *Handbook of Practical X-ray Fluorescence Analysis*, edited by B. Beckhoff, B. Kanngieber, N. Langhoff, R. Wedell and H. Wolff, pp. 442-462. Berlin, Spinger-Verlag.

MARCOSA, M. M., HARRISON, M. R., SCHUHMACHER, M., DOMINGO, L. J. & PONGPIACHAN, S. (2010). *Sci. Total. Environ*. **408**, 2387-2393.
MATSUMARU, R., NAGAMI, K. & TAKEYA, K. (2012). *IATSS. Res*. **36 (1)**, 11-19.
PONGPIAJUN, S. (2006). Atmospheric Chemistry of Semi-Volatile Organic Compounds in Urban and Rural Air, University of Birmingham.
PONGPIACHAN, S., THUMANU, K., KOSITANONT, C., SCHWARZER, K., PRIETZEL, J., HIRUNYATRAKUL, P. & KITTIKOON, I. (2012). *J. Anal. Methods. Chem*. Article ID 659858, doi: 10.1155/2012/659858.
PONGPIACHAN, S., THUMANU, K., NA PHATTHALUNG, W., TIPMANEE, D., KANCHAI, P., FELDENS, P & SCHWARZER, K. (2013). *Sci. Tsu. Haz.* (ISSN 8775-6839), **32 (1)**, 39-57.
SAKUNA, D., SZCZUCIŃSKI, W., FELDENS, P., SCHWARZER, K. & KHOKIATTIWONG, S. (2012). *Earth. Planets. Space*. **64**, 931-943.
SOLE, V. A., PAPILLON, E., COTTE, M., WALTER, PH., & SUSINI, J. (2007). *Spectrochim. Acta B*, **62**, 63-68.
SOONTARANON, S. & RUGMAI, S. (2012). Small angle X-ray scattering at Siam photon laboratory, *Chinese. J. Phys*. **50 (2)**, 204–210, 2012.
SZCZUCIŃSKI, W., NIEDZIELSKI, P., RACHLEWICZ, G., SOBCZYŃSKI, T., ZIOŁA, A., KOWALSKI, A., LORENC, S. & SIEPAK, J. (2005). *Environ. Geol*. **49 (2)**, 321-331.
SZCZUCIŃSKI, W., CHAIMANEE, N., NIEDZIELSKI, P., RACHLEWICZ, G., SAISUTTICHAI, D., TEPSUWAN, T., LORENC, S. & SIEPAK, J. (2006). *Pol. J. Environ. Stud*. **15 (5)**, 793–810.
SZCZUCIŃSKI, W., NIEDZIELSKI, P., KOZAK, L., FRANKOWSKI, M., ZIOŁA, A. & LORENC, S. (2007). *Environ. Geol*. **53 (2)**, 253-264.
SZCZUCIŃSKI, W. (2012). *Nat. Hazards Earth Syst*. *Sci*. **60**,115–133.
TANCHARAKORN, S., TANTHANUCH, W., KAMONSUTTHIPAIJIT, N., WONGPRACHANUKUL, N., SOPHON, M., CHAICHUAY, S., UTHAISAR, C. & YIMNIRUN, R. (2012). *J. Synchrotron. Rad*. **19**, 536-540.
TIPMANEE, D., DEELAMAN, W., PONGPIACHAN, S., SCHWARZER, K. & SOMPONGCHAIYAKUL, P. (2012). *Nat. Hazards Earth Syst. Sci*. **12**, 1441–1451.
VÖTT, A., LANG, F., BRÜCKNER, H., PAPANASTASSIOU, G. K., MAROUKIAN, H., PAPANASTASSIOU, D., GIANNIKOS, A., HADLER, H., HANDL, M., NTAGERETZIS, K., WILLERSHÄUSER, T. & ZANDER, A. (2011). *Quatern. Int*. **242(1)**, 213-239.

ISSN 8755-6839

SCIENCE OF TSUNAMI HAZARDS

Journal of Tsunami Society International

Volume 32 Number 2 2013

A NEW TSUNAMI RISK SCALE FOR WARNING SYSTEMS - APPLICATION TO THE BAY OF ALGIERS IN ALGERIA, WEST MEDITERRANEAN SEA

L. A. Amir

USTHB- FSTGAT, BP 32, El Alia, Bab Ezzouar, 16111, Algiers, Algeria

A. Cisternas

Universidad de Chile, Departamento de Geofisica, Casillo 2777, Santiago, Chile

W. Dudley

University of Hawaii at Hilo, 200W, Hilo, Hawaii, 96720 USA

B. G. McAdoo

Vassar College, Box 735, Poughkeepsie, NY, USA

G. Pararas-Carayannis

Tsunami Society International, Honolulu, Hawaii, USA

ABSTRACT

The city of Algiers and the surrounding coastal areas in northern Algeria are vulnerable to earthquakes which range from moderate to severe. In 2006, using several possible earthquake scenarios for the Western Mediterranean, the Japan International Cooperation Agency and the Algerian National Seismic Engineering Research Center predicted that heavy damage could occur in the Algiers region. Algerian Civil Defense authorities are particularly concerned by the threat of near-field earthquakes, associated slides and rock falls, as well as for tsunamis that can be generated. The present study proposes a new tsunami risk scale that provides information about the exposed communities and infrastructure, which can be used for regional tsunami alerts and warnings. Furthermore, it evaluates the vulnerability along the Bay of Algiers from tsunamigenic earthquakes. The JMA seismic intensity scale (Shindo scale) and the corresponding seismic peak ground accelerations are used in the evaluation. The results of tsunami modeling studies and of earthquake vulnerability assessment described by the present study, emphasize the significance of public education and preparedness in efforts to mitigate loss of life and damage to property.

Keywords: *vulnerability, earthquakes, tsunami, risk, Bay of Algiers, Algeria*

Vol. 32, No. 2, page 116 (2013)

1. INTRODUCTION

Algiers is the capital of Algeria and its primary harbor. A 2009 report states that the city has a population of more than 3 million inhabitants (source: www.ons.dz). Situated at the limit between the Africa and European convergent tectonic plates, the seismic risk is high for this region and the tsunami hazard has been evaluated and well documented from the XIVth century to present day (Roger et al., 2008, 2011; Ambraseys and Vogt, 1988; Amir et al, 2012). By the XIVth century, the defenses of the city of Algiers were totally related to the defense of the naval forces and consequently to the consolidation and development of fortified structures within the harbor (Belhamissi, 2009). The harbor was further consolidated with walls, in order to protect ships from bad weather conditions (Diego de Haëdo, 2004). Today, the harbor is saturated because of high maritime traffic (freight and human transportation to/from Europe).

The severity of a disaster's impact along coastal Algerian cities is strongly related to: (1) urban planning; (2) the density of the population; and (3) the implementation and efficiency of prevention/education policies. The Algiers region is located in the central part of the country and extends over an area of 2730 km^2. The Bay of Algiers covers a distance of about 30 km from East to West. If a tsunami is generated in the region, immediate measures must be taken to rapidly evacuate people of coastal areas to higher ground. The challenge is mostly related in finding vertical evacuation infrastructures that are built in accordance to seismic safety rules, in designating roads for evacuation and in establishing shelters where people can be protected from maximum tsunami inundation. Specific problems which must be addressed, include traffic issues, potentially collapsed bridges, blocked roads and alternate evacuation routes.

In 2006, the Japan International Cooperation Agency and the CGS published a report that revealed the potential damage from a list of earthquake scenarios. Six active faults were identified in the Algiers region (JICA and CGS, 2006). In particular, the report noted that an earthquake with a magnitude of M_W 6.8 along the offshore fault of Kheireddine could inflict most of the structural damage in the central and western part of the Bay of Algiers. Furthermore, the report postulated that 22 bridges would collapse or suffer destruction and that the harbor would be highly affected. In that context, for a tsunami triggered by an earthquake along this fault, the key issue is to determine the vulnerability of coastal sites and to educate people living in such areas, to quickly evacuate to higher elevation immediately when they feel the ground shaking. Unfortunately, the western and central parts of Algiers Bay are the most vulnerable areas where numerous slums spread in recent years (Figure 1). During a tsunami disaster, people living in such areas have the highest level of risk and are likely to be greatly affected – thus needing protection. A 2009 report (Hoffman, 2009) stated: *"Vulnerable populations, also called "special needs" populations or "at risk" populations, are those that are particularly "at risk of poor physical, psychological or social health" after a disaster. They have additional needs before, during and after an incident in functional areas, including but not limited to maintaining independence, communication, transportation, supervision and medical care.*" Additionally, the report defined the categories of population potentially vulnerable during disasters to "*individuals with physical and mental disabilities, elderly persons, pregnant women, children, prisoners, economically disadvantaged minorities, undocumented workers and those with language barriers*".

Figure 1. Slum at the entrance of El Oued El Hamiz, Bordj El Bahri, Algiers bay, Algeria.

In view of the above-described vulnerabilities, the purpose of the present study is to develop a risk scale in the framework of a tsunami warning program. Thus, a disaster risk assessment method for Algiers Bay is specifically developed, based on the combined impact of earthquakes and of generated tsunamis that would affect the coast. A first attempt is to determine a vulnerability index, as developed and described in an earlier publication (Amir et al., 2012). Subsequently, additional consideration is given to vulnerability from seismic ground shaking, to the regional geology and to materials used for construction. By combining the tsunami risk to the seismic vulnerability, an attempt is made by this study to identify potentially weak vertical infrastructures and to quantify the population's exposure to the risk. Finally, tsunami parameters are estimated from a tsunami modelling study.

2. VULNERABILITY AND RISK SCALE

Assessment of risk from potential earthquakes and tsunamis is critical for populated coastal areas. The reports from the JICA and CGS (2006) support the premise that potential tsunami damage complicates planning and warning policies. With the growing of coastal infrastructure in vulnerable seismic areas, difficulties arise regarding the application of seismic safety rules and construction codes because of the high ground liquefaction potential. Furthermore, tsunami preparedness must include the previously stated objectives of rapid evacuation of people soon as the ground begins to shake and the designation of direct routes to safe shelters. Such policies are difficult to implement.

2.1 Tsunamigenic Earthquake Vulnerability Scale (TEV scale):

The first step in evaluating the vulnerability from a tsunamigenic earthquake is to establish a risk scale, based on realistic parameters that illustrate broad aspects of what can cause

damage. In European countries and in North Africa, the seismic intensity scale being used for macro seismic studies, is that known as EMS-98 or MSK. However, materials used for construction are not specified and not considered. Hence, it is difficult to assess either the seismic or the tsunami energy that may have destroyed infrastructure or fortifications in past centuries.

The second parameter that is not considered, relates to local geology. Specific geological conditions could induce ground liquefaction or alternatively could attenuate seismic ground shaking.

In the present study work, we used the Shindo scale of the Japanese Meteorological Agency (Epstein, 2011) to develop a "tsunamigenic earthquake vulnerability" (TEV) scale. This scale helps consider additional parameters necessary to evaluate the potential damage from a tsunamigenic earthquake and to provide warning systems with vulnerability details of which communities are at risk.

Tsunami warning systems are commonly based on a severity scale of four degrees, ranging from low degree to high. This scale includes a fifth degree with no tsunami potential at all. From the description of the earthquakes damage, structural materials and geology, the TEV scale is derived from the Shindo scale to highlight indicators of vulnerability for urban or rural regions. Hence, corresponding ranges for peak ground accelerations recorded immediately after the first shock can then be correlated to potential damages and, consequently, help establish the communities and population at risk. The TEV scale is divided into 5 degrees (see Table 1 in Appendix).

2.2 Tsunami Vulnerability Indicators and Tsunami Risk Scale

Tsunami vulnerability is strongly related to an earthquake's generation of near field tsunamis. In this section, we identify indicators that provide a ranking for tsunami vulnerability. The tsunami risk results from a combination of the hazard and the vulnerability. The physical parameters for the hazard include the initial wave height, the velocity/energy phase and the final coastal inundation and run-up heights.

The effects of tsunamis relative to damage from earthquakes were studied for northern Algeria (Amir et al., 2012). The index of vulnerability was estimated from the ratio of Tsunami Intensity (Papadopoulos and Imamura Scale) (12 degrees) (Papadopoulos and Imamura, 2001) relative to the Earthquake Seismic Intensity from the EMS-98 Scale (12 degrees). However, only water height, damage and estimated seismic intensity from reports and the literature were considered. Criteria such as construction materials, substrata and limited flooding, were not examined accurately to assess a rigorous vulnerability and to assign a risk scale. Only reported damage from past events helped determine that the vulnerability for earthquakes is higher than that for tsunamis.

In this work, we examined and correlated indicators from the Tsunami Intensity Scale of Papadopoulos and Imamura (2001) with the Shindo Scale. These indicators include impact of the tsunami on people, vessels, wooden structures, masonry buildings and reinforced concrete structures. Tsunami deposits, wave height and limited flooding are correlated as well in this scale. These represent valuable data that is needed for proper risk assessment. The present tsunami vulnerability study considers the indicators relative to the TEV, in addition to the classical tsunami vulnerability parameters (see Table 2 in the Appendix).

3. APPLICATION TO THE ALGIERS BAY

GPS coordinates of 18 points of interests (one for each coastal district) were measured along the shoreline of the Algiers Wilaya. These points either correspond to vulnerable places (slums, entrance of seismically vulnerable bridges) or to potential locations for population evacuation (funfair, gardens, etc).

3.1 Indicators of Vulnerability for the Algiers Region

As stated, urban population within the Algiers region is more than 3 million. Various civilizations from successive periods of colonialism and cultural dominations across centuries, have built structures and monuments that corresponded to materials and cultural architectures of their own. Many infrastructure facilities (hospitals, apartments, government buildings) were built prior 1962. At that time, seismic safety standard rules and seismic engineering codes were not yet well studied. It is only after the El Asnam Earthquake (October 1980, Ms= 7,3) that regulations began to be implemented.

Moreover, *"most of bridges in Algiers are reinforced concrete, composed of prefabricated and prestressed beams or steel beams supported by multiple columns piles. A large number of bridges have been built after 1980 without any seismic design."* (Lazzali and Farsi, 2009). In 2012, Lazzali and Farsi conducted a survey to match the buildings, infrastructure and private houses with seismic vulnerability classes. They used five vulnerability classes decreasing from A to E, deduced from the EMS-98 scale. Accordingly, classes A to C correspond to adobe houses, brick buildings and reinforced concrete structures with no earthquake resistant design. Classes D and E represent structures with earthquake resistant design (reinforced concrete, reinforced or confined masonry) (Lazzali and Farsi, 2012). The density of dwellings for the Algiers region is presented in a 2004 report (Belazougui et al., 2004). Which structures represent safe shelters for evacuation in case of a tsunami emergency is a very important policy decision. For example, most of the buildings in the center of Algiers are masonry buildings constructed prior to 1962, thus may not be safe.

The present study used this assessment of seismic vulnerability for the Algiers region and added the risk exposure based on the estimated population density (from Cheurfi, 2011) to provide full details of earthquake and tsunami vulnerability indicators for the eighteen coastal districts of Algiers (see Table 3 in Appendix).

3.3 Earthquakes Scenario and Tsunami Modelling for the Algiers Region

The Algerian coast has a high level of seismic vulnerability although tsunami damages have also been reported, observed and simulated. Mapping potential tsunami coastal inundations for vulnerable points is crucial in establishing evacuation policies and methodology for warning.

Identified active faults inland and offshore (JICA and CGS, 2006, 2007; Domzig et al., 2006) have the potential to trigger tsunamigenic earthquakes with magnitudes higher than 6.5 (Figure 2). Tsunami travel times for scenarios of offshore Algeria earthquake (M=7.5, off Algiers and Oran) were simulated in a previous paper (Amir and Cisternas, 2010; Amir et al. 2012) using the SWAN code, which solves the shallow water wave equations within a finite difference scheme (Mader, 2004). Whatever the scenario for near field tsunami along the Algerian coast (1,200 km in length), the travel times are in the same range of order. Tsunami

waves reach the Algerian coast in less than 5 minutes and the Balearic Islands and the Spanish coast about 15 to 20 minutes later. As for the French and Italian coasts, tsunami waves can be expected about 20 minutes to 30 minutes later (Alasset et al., 2006). Inundating waves at the shoreline can be simulated with the code Geoclaw (George and Leveque, 2006). This finite element package includes the Rieman solver for flooding critical issues onto dry land.

In the present work, earthquake scenarios related to the active Kheireddine, the Chenoua and the Zemmouri thrust faults were reconsidered for mapping coastal tsunami inundation. For all these faults, tests were conducted for earthquakes having strikes ranging between 40˚N to 70˚N. For the Kheireddine and the Zemmouri faults, the dips vary between 30˚ to 60˚ in the SE direction. The Tsunami Hazard parameters necessary to assess the tsunami risk include the initial height of the tsunami waves at the source and their arrival times and terminal velocities for the eighteen districts along the shoreline of the Algiers region. The topographic data being used for the calculations is from the ETOPO-1mn database (NGDC/NOAA, http://www.ngdc.noaa.gov) (Amante and Eakins, 2009).

The results show that the time delay is extremely short, mostly for the western part of the Algiers coast (from D1 to D8), but the heights of the estimated inundating waves are higher. The height of the inundating waves varies as well from D1 to D18. In fact, regardless of what is used as scenario (for earthquakes along the Zemmouri or Kheirddine faults), the impact of the tsunami wave velocity for vulnerable points is crucial. The estimated range of the tsunami runups is less than 2 meters in height. But the tsunami wave velocity varies according to the geomorphology of the coast (Figure 2).

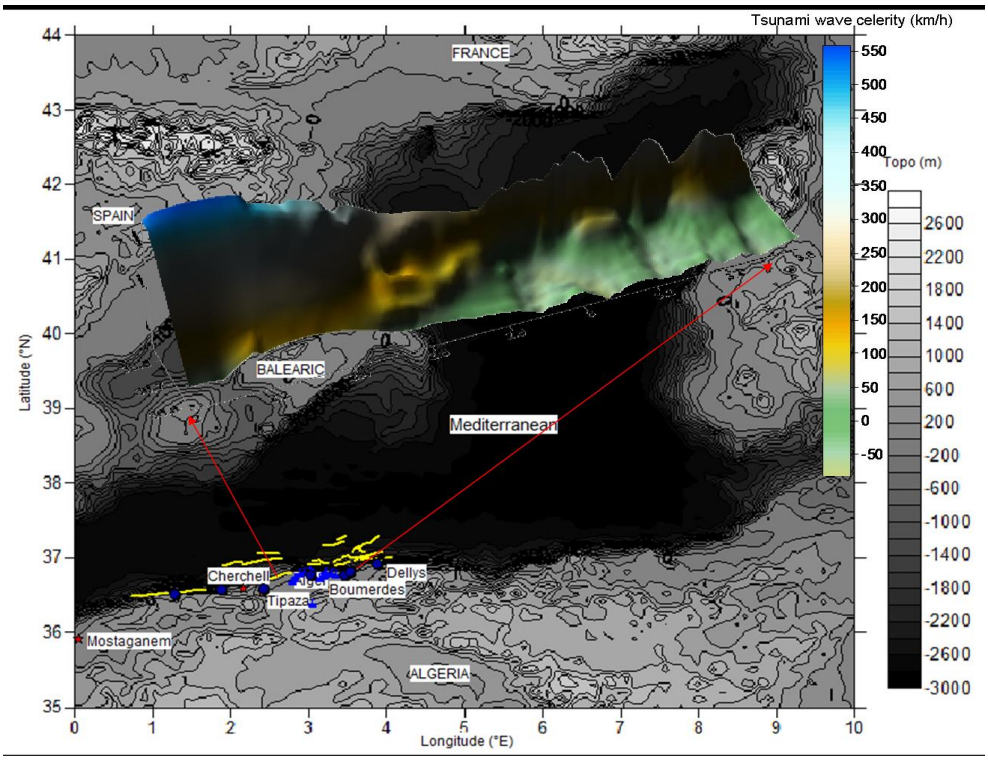

Figure 2: Tsunami Hazard Parameters for the Algiers Coast. The yellow lines represent the offshore faults (compiled after Mauffret et al., 1997, Domzig et al., 2006). The blue circles represent documented historical tsunamis from the NGDC-NOAA database. The blue flags represent the 18 points of interest measured along the coast.

These elements are very important in deciding where to place educational warning signs along coastal areas. The impact of tsunami waves traveling at 20 km/h on the boats of local fishermen is not the same as the impact of tsunami waves traveling at 50 km/h for the same elements (Figure 3).

Figure 3: Fishing boats of a vulnerable group.

4. TSUNAMI RISK ASSESSMENT FOR THE ALGIERS REGION

The tsunami risk is evaluated from the tsunami hazard parameters and the estimated TEV. From the peak ground accelerations (PGA) values, parameters such as the ground slope failures or structural damage can be "predicted", based on the Shindo scale and the tsunamigenic earthquake vulnerability.

The results integrate flooding due to potential liquefaction in the marshy lands or nearby rivers or the tsunami flooding. PGA values are from the JICA and CGS study (2006). Figure 4 represents the TEV and the Tsunami Risk (TR) estimated for the Heir Eddie EQ scenario (Mw= 7). The Tsunami Risk is evaluated for the 18 points of interest along the coastal area of Algiers. The results reflect either places of vulnerability or places for evacuation of people or are related to structures (informal or formal dwellings).

The Tsunami Risk is mostly low to moderate, except for the locations characterized as PI7, PI13 and PI14. For these three points of interest, the tsunami can be damaging. The soil is vulnerable to earthquake liquefaction and the dwellings are "informal" and located at the shoreline. Hence, the potential flooding due to a combination of earthquake impact, triggered

turbidity currents and the tsunami waves coming from the Kheir Eddine offshore epicentral area, may have an importance for a group which is already considered vulnerable from the definition of Hoffman (2009). On the other hand, even if the tsunami hazard is higher in the older part of the city (Algiers Center, Bologhine, Belouizdad), crucial issues in estimating the tsunami risk include: (1) the potential collapse of buildings due to their prior state of degradation, (2) the density of the dwellings, 3) traffic, and 4) the number of people exposed to earthquake vulnerability.

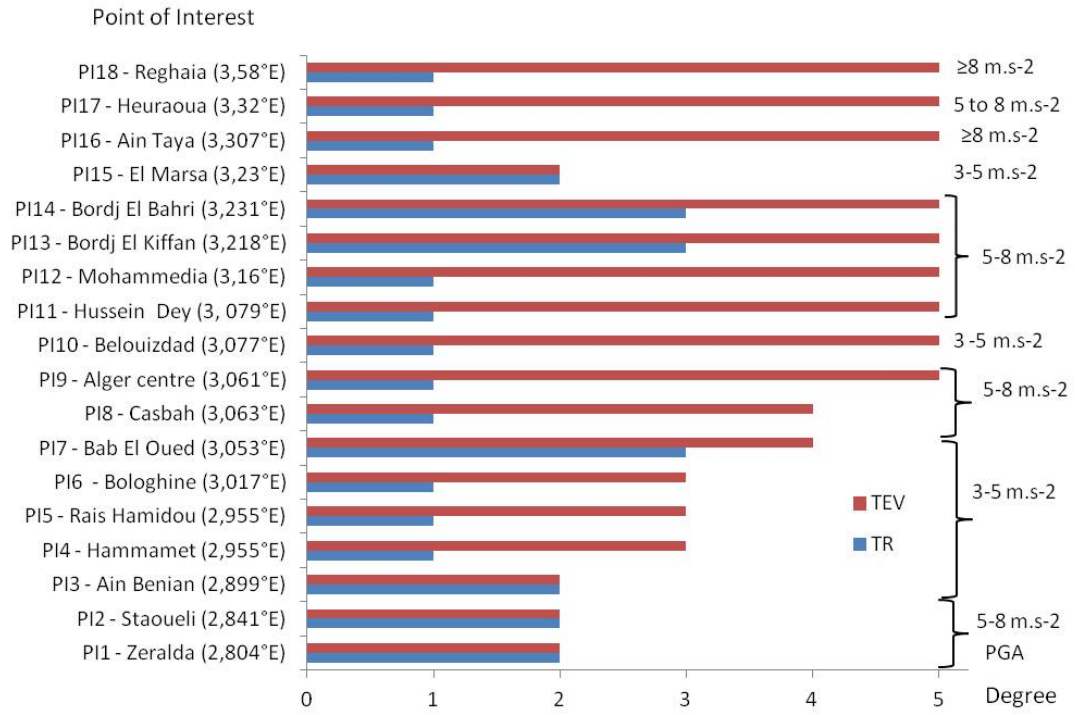

Figure 4. Tsunamigenic Earthquake Vulnerability (TEV) and Tsunami Risk estimated for the 18 Points of Interest in the Algiers Wilaya. Peak Ground Accceleration (PGA) values from JICA and CGS (2006) are reported.

5. DISCUSSIONS AND CONCLUSIONS

The city of Algiers is built amphitheatrically. The wealthier members of society reside at the higher levels of the city while the poorer people live at the lower level (slums of Bordj El Kiffan and Bordj El Bahri). More and more buildings are constructed with no control for seismic regulations or right distances between the shoreline and the private homes.

On the other hand, seawalls of 3 m in height exist in the harbor of Algiers and in the district of Ain Benian. The beaches at Ain Benian are located behind the seawall that only protects the harbor. The configurations of beaches differ along the Algiers coast. Along the Bay of Algiers, the beaches are urban. People who swim there belong to the "vulnerable group" (Figures 6, 7 and 8).

Figure 6. View of the district of Ain Benian (Harbor El Djemila, seawall height = 3m).

Figure 7. People walking along the path next the sea wall (2 – 3 m), eastern Algiers, road in the direction of Bologhine district.

Figure 8. Sea Wall (2 - 3 m) in front of the Popular Beach of Bab el Oued

Most of the structures in the Algiers region date back to periods of colonialism. In the older part of the city (Bologhine, Alger Centre, Bab El Oued, Belouizdad), the walls are already vulnerable because of the degree of degradation. The rehabilitation of older buildings is extremely difficult to attain. According to a 2008 UNEP report: *"The use of specific systems of knowledge and practices developed and accumulated over generations within a particular group and region reflects many experiences and problems solving"*.

ACKNOWLEDGEMENTS

This paper and work is dedicated to Prof. H. Benhallou who passed away in October 2011. He dedicated his life to seismic hazard analysis, disaster management and prevention and in education. Prof. Charles Mader (Mader Consulting & Co) is greatly acknowledged for his encouragement and technical assistance with the SWAN code.

REFERENCES

AMANTE, C. AND EAKINS, B. W. (2009), ETOPO 1 Arc-Minute Global Relief Model: Procedures, Data Sources and Analysis. *NOAA Technical Memorandum NESDIS NGDC-24*, 19 pp,

AMBRASEYS, N.N. AND VOGT, J. (1988), Material for the investigation of the seismicity of the region of Algiers. *European Earth. Eng.,* **3**, 16-29.

ALASSET, P.-J, HÉBERT, H., MAOUCHE, S., CALBINI, V. AND MEGHRAOUI, M. (2006), The Tsunami induced by the 2003 Zemmouri Earthquake (Mw=6.9): modelling and results, *Geophysical J. Int.,* 166, 213-226

AMIR, L AND CISTERNAS, A. (2010), Appraisal of the 1790 Alboran Tsunami source in the west mediterranean sea as inferred from numerical modelling: Insights for the tsunami hazard in Algeria, *ITS 4th*, Proceedings of the 9th U.S. National and 10th Canadian Conference on Earthquake Engineering

AMIR, L., CISTERNAS, A., VIGNERESSE, J.-L., DUDLEY, W., MCADOO, B., (2012), Algeria's vulnerability to tsunamis from near field seismic sources. *Science of Tsunami Hazards*, 31:1, 82-98

BELHAMISSI, M. (2009), Alger, la ville aux milles canons – Remparts et canons de la Casbah. Editions ANEP.

Belazougui, M, Farsi, M.N., Remas, A., Bensaibi, M., Mezazigh, B. (2004), Seismic risk assessment of current buildings of Algiers city, *13th WCEE*, Proceedings Paper No 3115

CHEURFI, A. (2011), Dictionnaire des localités algériennes. Casbah Editions.

DIEGO DE HAËDO (2004), Topographie et Histoire Générale d'Alger – La vie à Alger au seizième siècle. Ed. Grand-Alger-Livre.

DOMZIG, A., YELLES, K., LE ROY, C., DEVERCHERE, J., BOUILLIN, J.-P., BRACENE, R., MERCIER DE LEPINAY, B., LE ROY, P., CALAIS, E., KHERROUBI, A., GAULLIER, V., SAVOYE, B., PAUC, H. (2006), Searching for the Africa - Eurasia Miocene Boundary Offshore western Algeria (MARADJA'03 cruise). *C.R. Geosciences*, **338**, 80-91.

EPSTEIN, W. (2011), A Probabilistic Risk Assessment Practioner looks at the Great East Japan Earthquake and Tsunami, A Ninokata laboratory white paper, Tokyo Institute of Technology, Ninokata laboratory, 55 p.

HOFFMAN, S. (2009), Preparing for disaster: Protecting the most vulnerable in emergencies, *UC Davis Law Review*, 42, 1491-1547.

JICA AND CGS (2006), A Study of Seismic Microzoning of the wilaya of Algiers in the People's Democratic Republic of Algeria, Final Report, **2**, Oyo International Corp. Nippon Koei Co., Ltd.

JICA AND CGS (2007), Microzonage du Risque Sismique de la Wilaya d'Alger. 7ieme Colloque National AFPS, 13 p.

LAZZALI, F. AND FARSI, M. (2009), Seismic Vulnerability of bridges and traffic disruption within Algiers city. *International Journal of Applied Engineering Research*, **4**,931-944.

LAZZALI, F. AND FARSI, M. (2012), Seismic Vulnerability Assessment of Buildings in Algiers Area. *World Academy of Science, Engineering and Technology*, **61,** 796-800.

MAUFFRET, A. (2007), The Northwestern (Maghreb) boundary of the Nubia (Africa) plate. Tectonophysics. 429, 21-44.

MADER, C.L. (2004), Numerical Modeling of Water Waves, second edition, CRC Press, 269 pp.

PAPADOPOULOS, G. A. AND IMAMURA, F. (2001), A proposal for a new tsunami intensity scale, *ITS 2001*. Proceedings session 5 : 5-1 : 569-577

ROGER, J., HÉBERT, H. (2008), The 1856 Djijelli (Algeria) earthquake and tsunami: source parameters and implications for tsunami hazard in the Balearic Islands. *Natural Hazards and Earth System Sciences*, 8:4, 721-731

ROGER, J., HÉBERT, H., RUEGG, J.C. AND BRIOLE, P. (2011), The El Asnam 1980 October 10 inland earthquake: a new hypothesis of tsunami generation. *Geophys. J. Int.*, 185:3, 1135-1146.

UNEP (2008), Indigenous knowledge in Disaster Management in Africa, Chapter 2, Publication compiled and edited by Peter Mwaura.

Appendix – Tables

Table 1: Tsunamigenic Earthquake Vulnerability Scale (TEV scale); LP: Liquefaction Potential; RS: Rock Slide; F: Flooding; CV: Class Vulnerability; AS: Available Space to evacuate.

Rank	Indicators of Vulnerability						Shindo Scale	PGA (m/s^2)
	Physical			Buildings		Population Exposure		
	LP	RS	F	CV	AS			
1: Very Unlikely							1(1) to 2(2) / 0.5-2.4	0.008 to 0.08
2: Unlikely							3 (3) / 2.5-3.4	0.08 to 0.25
3: Possible							4 (4) / 3.5-4.4	0.25 to 0.8
4: Likely							5-lower to 5-upper/ 4.5-5.4	0.8 to 2.5
5: Very Likely							6-lower to 7 (7) / 5.5 and up	≥ 2.5

Table 2: The Tsunami Risk Scale

Score	Vulnerability		Shindo Scale	Papadopoulos-Imamoura Tsunami Intensity Scale
	Physical	Structural & Population		
0: No Risk			1(1) to 2(2) / 0.5-2.4	1 (I)
1: low			3 (3) / 2.5-3.4	2 (II) – 4 (IV)
2: moderate			4 (4) / 3.5-4.4	5 (V) – 7 (VII)
3: destructive			5-lower to 5-upper/ 4.5-5.4	8 (VIII) – 9 (IX)
4: catastrophic			6-lower to 7 (7) / 5.5 and up	10 (X) – 12 (XII)

Table 3: Tsunami vulnerability indicators in Algiers; (a) SC (classification of sites from the Algerian seismic code RPA99-2003): S1 (rocky site); S2 (firm site); S3 (soft site); S4 (very soft site) s; (a) SC for classification of sites (Algerian seismic code RPA99-version 2003): S1 (rocky site); S2 (firm site); S3 (soft site); S4 (very soft site)

District	VC (Lazzali et Farsi, 2012)	Exposed area & population (www.ons.dz; Cheurfi, 2011)		Geology (compiled after the Cheragas and Algiers Geological Map-scale : 1/50 000)	Site Classification SC (a)
		Pop (1998)	Area (km^2)		
Zeralda (D1)	B	18183	31,46	Beaches, dunes (recent & consolidated), shaly sand, shale & clays, sandy & shaly-sand facies	S3; S4
Staoueli (D2)	C	35241	22,23	beaches, dunes (recent & consolidated), gneiss, marshy & lacustrine deposits, shaly sand, coquina, pudding stone & marine sandstones	S3; S4
Ain Benian (D3)	B	50756	13.26	Beaches, dunes (recent & consolidated), coquina, pudding stone & marine sandstones.	S3; S4
Hammamet (D4)	B	19651	8.6	Beaches, consolidated dunes, shaly sand, shales and clays, sandy & shaly-sand facies	S3; S4
Rais Hamidou (D5)	B	21518	4.94	Beaches, schist (lens of limestone), gneiss	S1
Bologhine (D6)	A	43283	2.76	Beaches, schist (lens of limestone), gneiss	S1

Bab El Oued (D7)	B	87557	1.2	Beaches, schist (lens of limestone), alluviums; shaly sand.	S1; S2
Casbah (D8)	A	50453	9000 m2	Schist (lens of limestone).	S1;
Alger centre (D9)	B	96329	3.70	Mica schists, shaly sand, schists (lens of limestones)	S1; S2; S3
Belouizdad (D10)	A	91482 (2002)	2.16	Beaches, shaly sands, limestone; lutetian limestone with bivalvia.	S1; S2; S3
Hussein Dey (D11)	B	49921	49	beaches, dunes (recent & consolidated); shaly sand	S3; S4
Mohammadia (D12)	C	42079	7.9	Beaches, dunes (recent & consolidated); shaly sand; marine deposits with small quartz pebbles and red sands, pudding stone & coarse sandstones; ancient alluviums.	S3;S4
Bordj El Kiffan (D13)	B	143000 (2009)	21.7	Beaches, dunes (recent & consolidated); shaly sand; marshy and lacustrine deposits; marine deposits with small quartz pebbles and red sands, pudding stone & coarse sandstones;	S3; S4
Bordj El Bahri (D14)	B	27905	7.5	Beaches, dunes (recent & consolidated); shaly sand; marshy and lacustrine deposits; coquina; pudding stone and marine sandstone; marine	S3; S4

				deposits with small quartz pebbles and red sands, pudding stone & coarse sandstones;	
El Marsa (D15)	B	8783	3.9	Shists, schists (lens of limestones), gneiss, shaly sand, sandstone facies	S1,S2,S3,S4
Aïn Taya (D16)	B	28430	9.55	beaches, shaly sand, marine deposits with small quartz pebbles and red sands, pudding stone & coarse sandstones;	S3; S4
Heuraoua (D17)	B	18121	13	Alluviums, marchy & lacustrines deposits, consolidated dunes, shaly sands	S4
Reghaia (D18)	B	62474	26.3	Alluviums, marshy & lacustrines deposits, consolidated dunes.	S4

ISSN 8755-6839

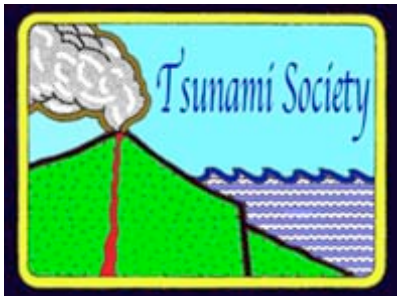

SCIENCE OF **TSUNAMI HAZARDS**

Journal of Tsunami Society International

Volume 32 **Number 2** **2013**

TSUNAMI SOCIETY INTERNATIONAL, 1741 Ala Moana Blvd. #70, Honolulu, HI 96815, USA.

WWW.TSUNAMISOCIETY.ORG